









TECH BRIEFS

NATIONAL AERONAUTICS AND SPACE ADMINISTRATION

-  Technology Focus
-  Electronics/Computers
-  Software
-  Materials
-  Mechanics/Machinery
-  Manufacturing
-  Bio-Medical
-  Physical Sciences
-  Information Sciences
-  Books and Reports

INTRODUCTION

Tech Briefs are short announcements of innovations originating from research and development activities of the National Aeronautics and Space Administration. They emphasize information considered likely to be transferable across industrial, regional, or disciplinary lines and are issued to encourage commercial application.

Availability of NASA Tech Briefs and TSPs

Requests for individual Tech Briefs or for Technical Support Packages (TSPs) announced herein should be addressed to

National Technology Transfer Center

Telephone No. **(800) 678-6882** or via World Wide Web at <http://www.nttc.edu/about/contactus.asp>

Please reference the control numbers appearing at the end of each Tech Brief. Information on NASA's Innovative Partnerships Program (IPP), its documents, and services is also available at the same facility or on the World Wide Web at <http://ipp.nasa.gov>.

Innovative Partnerships Offices are located at NASA field centers to provide technology-transfer access to industrial users. Inquiries can be made by contacting NASA field centers listed below.

NASA Field Centers and Program Offices

Ames Research Center
Lisa L. Lockyer
(650) 604-1754
lisa.l.lockyer@nasa.gov

Dryden Flight Research Center
Gregory Poteat
(661) 276-3872
greg.poteat@dfrc.nasa.gov

Glenn Research Center
Kathy Needham
(216) 433-2802
kathleen.k.needham@nasa.gov

Goddard Space Flight Center
Nona Cheeks
(301) 286-5810
nona.k.cheeks@nasa.gov

Jet Propulsion Laboratory
Ken Wolfenbarger
(818) 354-3821
james.k.wolfenbarger@jpl.nasa.gov

Johnson Space Center
Michele Brekke
(281) 483-4614
michele.a.brekke@nasa.gov

Kennedy Space Center
David R. Makufka
(321) 867-6227
david.r.makufka@nasa.gov

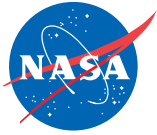
Langley Research Center
Martin Waszak
(757) 864-4015
martin.r.waszak@nasa.gov

Marshall Space Flight Center
Jim Dowdy
(256) 544-7604
jim.dowdy@msfc.nasa.gov

Stennis Space Center
John Bailey
(228) 688-1660
john.w.bailey@nasa.gov

Carl Ray, Program Executive
Small Business Innovation
Research (SBIR) & Small
Business Technology
Transfer (STTR) Programs
(202) 358-4652
carl.g.ray@nasa.gov

Doug Comstock, Director
Innovative Partnerships
Program Office
(202) 358-2560
doug.comstock@nasa.gov



TECH BRIEFS

NATIONAL AERONAUTICS AND SPACE ADMINISTRATION



Technology Focus: Sensors

- 5 The Radio Frequency Health Node Wireless Sensor System
- 6 Effects of Temperature on Polymer/Carbon Chemical Sensors
- 6 Small CO₂ Sensors Operate at Lower Temperature
- 7 Tele-Supervised Adaptive Ocean Sensor Fleet



Electronics/Computers

- 9 Synthesis of Submillimeter Radiation for Spectroscopy
- 10 100-GHz Phase Switch/Mixer Containing a Slot-Line Transition
- 11 Generating Ka-Band Signals Using an X-Band Vector Modulator
- 12 SiC Optically Modulated Field-Effect Transistor
- 12 Submillimeter-Wave Amplifier Module With Integrated Waveguide Transitions
- 13 Metrology System for a Large, Somewhat Flexible Telescope
- 14 Economical Implementation of a Filter Engine in an FPGA



15 Manufacturing & Prototyping

- 15 Improved Joining of Metal Components to Composite Structures
- 16 Machined Titanium Heat-Pipe Wick Structure



17 Materials

- 17 Gadolinia-Doped Ceria Cathodes for Electrolysis of CO₂



19 Mechanics/Machinery

- 19 Utilizing Ocean Thermal Energy in a Submarine Robot
- 20 Fuel-Cell Power Systems Incorporating Mg-Based H₂ Generators
- 21 Alternative OTEC Scheme for a Submarine Robot



23 Bio-Medical

- 23 Sensitive, Rapid Detection of Bacterial Spores
- 23 Adenosine Monophosphate-Based Detection of Bacterial Spores



25 Physical Science

- 25 Silicon Microleaks for Inlets of Mass Spectrometers
- 26 CGH Figure Testing of Aspherical Mirrors in Cold Vacuums
- 27 Series-Coupled Pairs of Silica Microresonators
- 28 Precise Stabilization of the Optical Frequency of WGMRs
- 29 Formation Flying of Components of a Large Space Telescope
- 29 Laser Metrology Heterodyne Phase-Locked Loop
- 29 Spatial Modulation Improves Performance in CTIS



31 Information Sciences

- 31 High-Performance Algorithm for Solving the Diagnosis Problem
- 32 Truncation Depth Rule-of-Thumb for Convolutional Codes
- 32 Efficient Method for Optimizing Placement of Sensors

This document was prepared under the sponsorship of the National Aeronautics and Space Administration. Neither the United States Government nor any person acting on behalf of the United States Government assumes any liability resulting from the use of the information contained in this document, or warrants that such use will be free from privately owned rights.



The Radio Frequency Health Node Wireless Sensor System

The system can be configured before or during operation.

John F. Kennedy Space Center, Florida

The Radio Frequency Health Node (RFHN) wireless sensor system differs from other wireless sensor systems in ways originally intended to enhance utility as an instrumentation system for a spacecraft. The RFHN can also be adapted to use in terrestrial applications in which there are requirements for operational flexibility and integrability into higher-level instrumentation and data-acquisition systems.

As shown in the figure, the heart of the system is the RFHN, which is a unit that passes commands and data between (1) one or more commercially available wireless sensor units (optionally, also including wired sensor units) and (2) command and data interfaces with a local control computer that may be part of the spacecraft or other engineering system in which the wireless sensor system is installed. In turn, the local control computer can be in radio or wire communi-

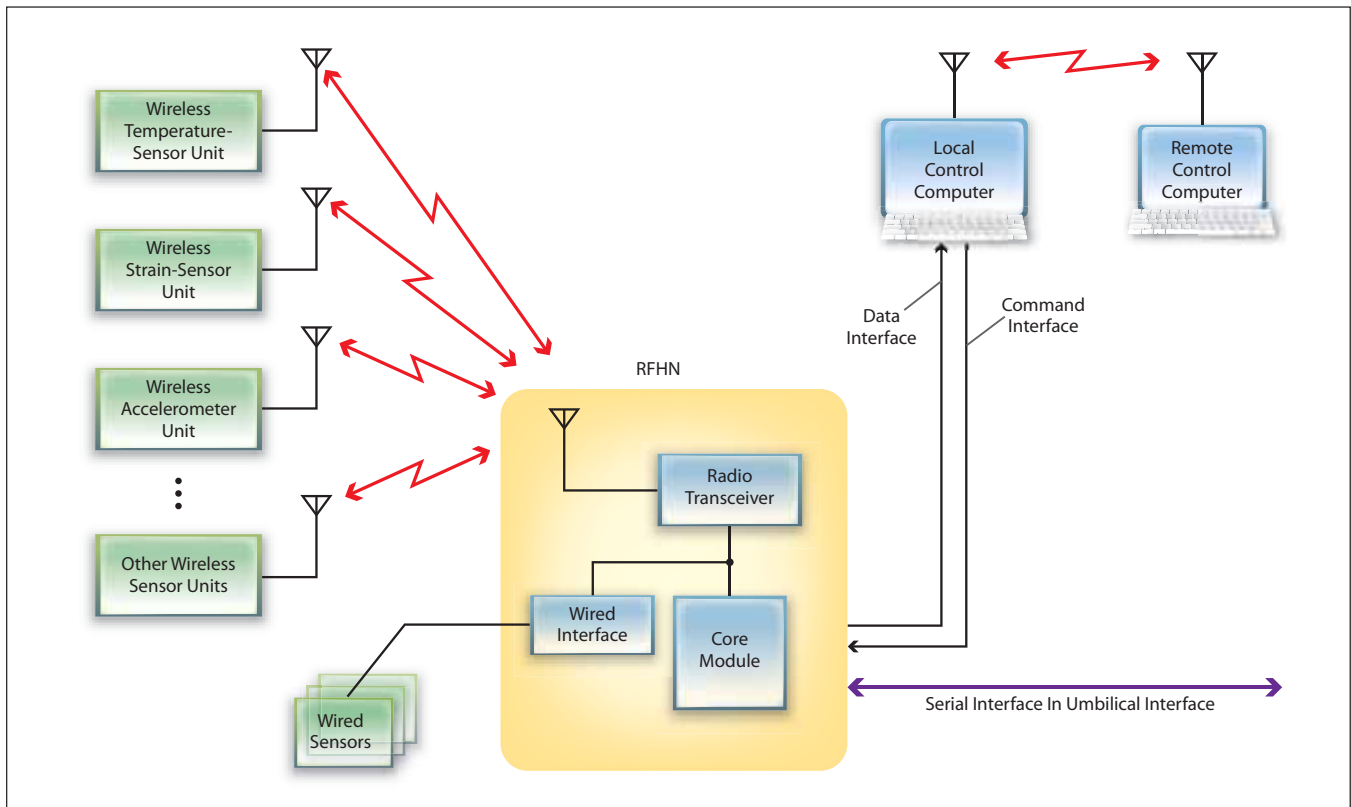
cation with a remote control computer that may be part of a higher-level system. The remote control computer, acting via the local control computer and the RFHN, cannot only monitor readout data from the sensor units but can also remotely configure (program or reprogram) the RFHN and the sensor units during operation. In a spacecraft application, the RFHN and the sensor units can also be configured more nearly directly, prior to launch, via a serial interface that includes an umbilical cable between the spacecraft and ground support equipment. In either case, the RFHN wireless sensor system has the flexibility to be configured, as required, with different numbers and types of sensors for different applications.

The RFHN can be used to effect real-time transfer of data from, and commands to, the wireless sensor units. It can also store data for later retrieval by

an external computer. The RFHN communicates with the wireless sensor units via a radio transceiver module. The modular design of the RFHN makes it possible to add radio transceiver modules as needed to accommodate additional sets of wireless sensor units.

The RFHN includes a core module that performs generic computer functions, including management of power and input, output, processing, and storage of data. In a typical application, the processing capabilities in the RFHN are utilized to perform preprocessing, trending, and fusion of sensor data. The core module also serves as the unit through which the remote control computer configures the sensor units and the rest of the RFHN.

This work was done by J. Emilio Valencia, Priscilla C. Stanley, and Paul J. Mackey of Kennedy Space Center. Further information is contained in a TSP (see page 1). KSC-12798



The RFHN is a communication, storage, and processing terminal that relays data from, and commands to, sensor units.

Effects of Temperature on Polymer/Carbon Chemical Sensors

NASA's Jet Propulsion Laboratory, Pasadena, California

Experiments were conducted on the effects of temperature, polymer molecular weight, and carbon loading on the electrical resistances of polymer/carbon-black composite films. The experiment were performed in a continuing effort to develop such films as part of the JPL Electronic Nose (ENose), that would be used to detect, identify, and quantify parts-per-million (ppm) concentration levels of airborne chemicals in the space shuttle/space station environments. The polymers used in this study were three formulations of poly(ethylene oxide) [PEO] that had molecular weights of 20 kilodaltons, 600 kilodaltons, and 1 megadalton, respectively.

The results of one set of experiments showed a correlation between the poly-

mer molecular weight and the percolation threshold. In a second set of experiments, differences among the temperature dependences of resistance were observed for different carbon loadings; these differences could be explained by a change in the conduction mechanism.

In a third set of experiments, the responses of six different polymer/carbon composite sensors to three analytes (water vapor, methanol, methane) were measured as a function of temperature (28 to 36°C). For a given concentration of each analyte, the response of each sensor decreased with increasing temperature, in a manner different from those of the other sensors.

This work was done by Allison Manfreda, Liana Lara, April Jewell, Margie Homer,

Shiao-Pin Yen, Adam Kisor, Margaret Ryan, Hanying Zhou, Abhijit Shevade, and Lim James of Caltech and Kenneth Manatt of Santa Barbara Applied Research for NASA's Jet Propulsion Laboratory.

In accordance with Public Law 96-517, the contractor has elected to retain title to this invention. Inquiries concerning rights for its commercial use should be addressed to:

Innovative Technology Assets Management
JPL

Mail Stop 202-233

4800 Oak Grove Drive

Pasadena, CA 91109-8099

(818) 354-2240

E-mail: iaoffice@jpl.nasa.gov

Refer to NPO-40621, volume and number of this NASA Tech Briefs issue, and the page number.

Small CO₂ Sensors Operate at Lower Temperature

Lower operating temperature translates to lower power demand.

John H. Glenn Research Center, Cleveland, Ohio

Solid-electrolyte-based amperometric sensors for measuring concentrations of CO₂ in air are being developed for use in detection of fires, environmental monitoring, and other applications where liquid-based electrochemical cells are problematic. These sensors are small (sizes of the order of a millimeter), are robust, are amenable to batch fabrication at relatively low cost, and exhibit short response times (seconds) and wide detection ranges.

A sensor of this type at a previous stage of development included a solid electrolyte of Na₃Zr₂Si₂PO₁₂ deposited mainly between interdigitated Pt electrodes on an alumina substrate, all overcoated with an auxiliary solid electrolyte of (Na₂CO₃:BaCO₃ in a molar ratio of 1:1.7). It was necessary to heat this device to a temperature as high as 600 °C to obtain the desired sensitivity and rapid response. Heating sensors increases the power consumption of the sensor system and complicates the use of the sensor in some applications. Thus, decreasing a sensor's power consumption while maintaining its performance is a technical goal of ongoing development.

A sensor of this type at the present state of development (see Figure 1) has

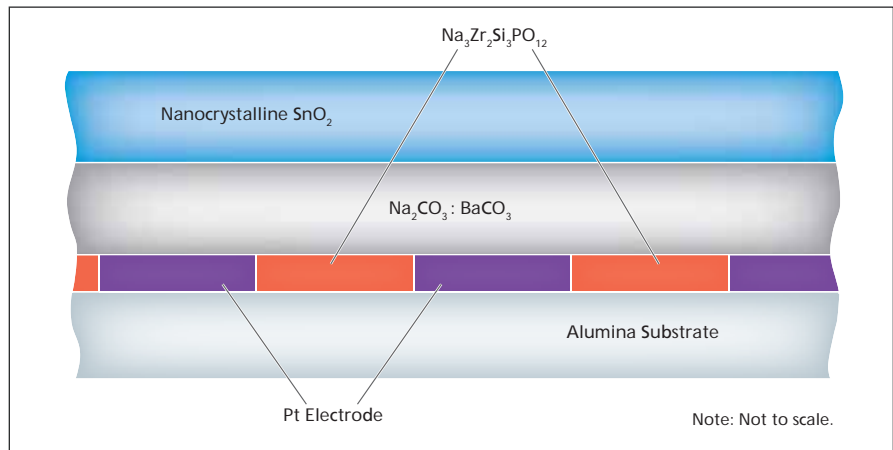


Figure 1. The Layer of Nanocrystalline SnO₂ enhances the function of the solid-electrolyte layers of Na₃Zr₂Si₂PO₁₂ and Na₂CO₃:BaCO₃, making it possible to operate at a lower temperature.

the same basic structure, except that it includes an additional outer layer of nanocrystalline SnO₂, which is an n-type (electron-donor-type) semiconductor that provides additional electrons for reduction reaction at the working electrode to detect CO₂. [This use of SnO₂ as a CO₂-sensor material should not be confused with the use of SnO₂ in a related development described in "CO₂ Sensors Based on Nanocrystalline SnO₂ Doped With CuO" (LEW-18247-1), NASA Tech Briefs, Vol 32, No. 10 (October 2008), page 44. The SnO₂ layer

makes it possible to obtain the desired sensor responses at a lower temperature (355 °C), thereby making it possible to operate the sensor at lower power. Figure 2 shows the comparison in response between a sensor with and without the armor layer of nanocrystalline SnO₂. Concentrations of CO₂ from 0.5 to 4% in air were also detected at 375 °C.

A sensor of this type can be fabricated in the following sequence:

1. The platinum interdigitated electrodes, typically having width and spacing of 30 μm, are formed on the

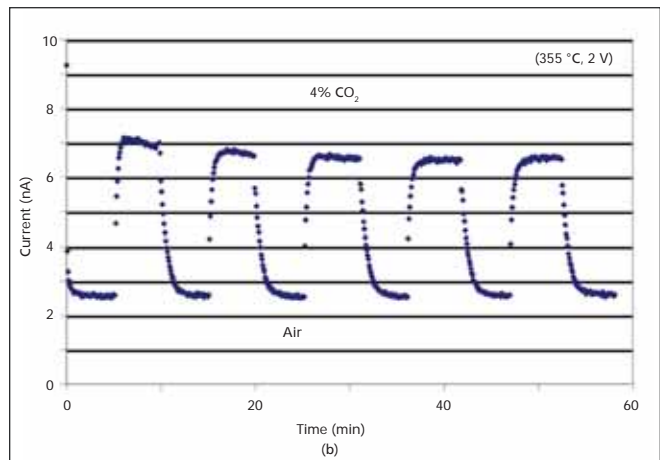
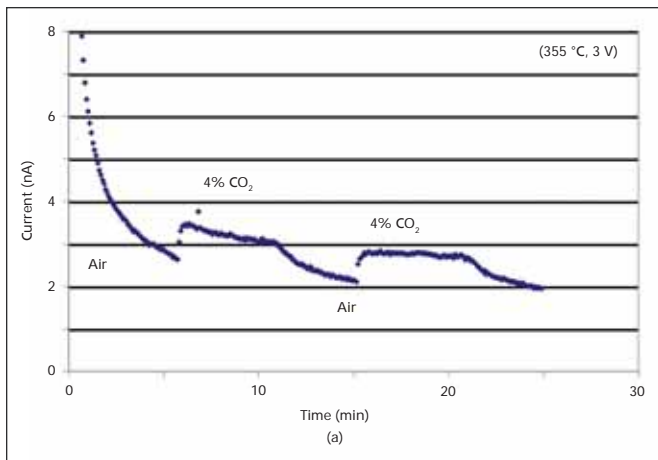


Figure 2. The Current Response of a CO₂ Sensor fabricated as described in the text was measured at an applied potential at a temperature of 355 °C. Figure 2(a) shows a CO₂ sensor response without a nanocrystalline SnO₂ coating, while Figure 2(b) shows a dramatic difference enabled by the addition of a coating of nanocrystalline SnO₂.

1. alumina substrate by use of standard techniques of sputter deposition, photolithography, and liftoff.
2. In a second process involving the use of standard techniques of sputter deposition, photolithography, and liftoff, the Na₃Zr₂Si₂PO₁₂ solid electrolyte is deposited mainly between (and touching) the platinum interdigitated electrodes.
3. The workpiece is heated to a temperature of 850 °C for 2 hours.
4. The Na₂CO₃:BaCO₃ auxiliary solid electrolyte is deposited on the electrodes and the Na₃Zr₂Si₂PO₁₂ solid

5. electrolyte by sputtering through a shadow mask.
 5. The workpiece is heated to 686 °C for 10 minutes, then to 710 °C for 20 minutes.
 6. The layer of nanocrystalline SnO₂ is deposited on the Na₂CO₃:BaCO₃ layer by a sol-gel process.
 7. The workpiece is heated to 500 °C for 2 hours.
- The workpiece is then ready for use as an amperometric CO₂ sensor. Research will continue to optimize CO₂ sensor performance, while decreasing the operating temperature and power consumption. The objective of

future work is to decrease the power consumption to enable, for example, long-term battery operation of CO₂ sensor systems.

This work was done by Gary W. Hunter and Jennifer C. Xu of Glenn Research Center. Further information is contained in a TSP (see page 1).

Inquiries concerning rights for the commercial use of this invention should be addressed to NASA Glenn Research Center, Innovative Partnerships Office, Attn: Steve Fedor, Mail Stop 4-8, 21000 Brookpark Road, Cleveland, Ohio 44135. Refer to LEW-18324-1

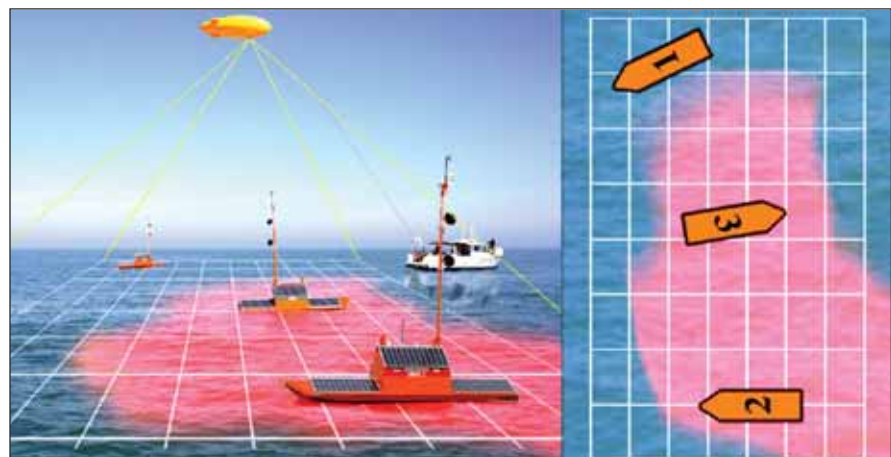
🌀 Tele-Supervised Adaptive Ocean Sensor Fleet

A software architecture and system deploys robotic boats to study ocean surface and subsurface phenomena such as coastal pollutants, oil spills, and hurricanes.

NASA's Jet Propulsion Laboratory, Pasadena, California

The Tele-supervised Adaptive Ocean Sensor Fleet (TAOSF) is a multi-robot science exploration architecture and system that uses a group of robotic boats (the Ocean-Atmosphere Sensor Integration System, or OASIS) to enable *in-situ* study of ocean surface and subsurface characteristics and the dynamics of such ocean phenomena as coastal pollutants, oil spills, hurricanes, or harmful algal blooms (HABs). The OASIS boats are extended-deployment, autonomous ocean surface vehicles. The TAOSF architecture provides an integrated approach to multi-vehicle coordination and sliding human-vehicle autonomy.

One feature of TAOSF is the adaptive re-planning of the activities of the OASIS vessels based on sensor input



A concept of the TAOSF Field Deployment System shows an overhead aerostat (an unmanned blimp tethered to a manned field operations vessel) that provides a global camera overview of three OASIS platforms and a patch of rhodamine dye. The overhead map is shown on the right.

(“smart” sensing) and sensorial coordination among multiple assets. The architecture also incorporates Web-based communications that permit control of the assets over long distances and the sharing of data with remote experts. Autonomous hazard and assistance detection allows the automatic identification of hazards that require human intervention to ensure the safety and integrity of the robotic vehicles, or of science data that require human interpretation and response. Also, the architecture is designed for science analysis of acquired data in order to perform an initial onboard assessment of the presence of specific science signatures of immediate interest.

TAOSF integrates and extends five subsystems developed by the participating institutions: Emergent Space Technologies, Wallops Flight Facility, NASA’s Goddard Space Flight Center (GSFC), Carnegie Mellon University, and Jet Propulsion Laboratory (JPL). The OASIS Autonomous Surface Vehicle (ASV) system, which includes the vessels as well as the land-based control and communications infrastructure developed for them, controls the hardware of each platform (sensors, actuators, etc.), and also provides a low-level waypoint navigation capability. The Multi-Platform Simulation Environment from

GSFC is a surrogate for the OASIS ASV system and allows for independent development and testing of higher-level software components. The Platform Communicator acts as a proxy for both actual and simulated platforms. It translates platform-independent messages from the higher control systems to the device-dependent communication protocols. This enables the higher-level control systems to interact identically with heterogeneous actual or simulated platforms.

The Adaptive Sensor Fleet (ASF) provides autonomous platform assignment and path planning for area coverage, as well as monitoring of mission progress. The System Supervision Architecture (SSA) provides high-level planning, monitoring, tele-supervision, and science data analysis. The latter is done using the Inference Grid (IG) framework to represent multiple spatially- and temporally-varying properties. The Inference Grid is a probabilistic multi-property spatial lattice model, where sensor information is stored in spatially and temporally registered form, and which is used for both scientific inferences and for vehicle mission planning. The information in each Inference Grid cell is represented as a stochastic vector, and metrics such as entropy are used to measure the uncertainty in the IG. The

IG is used for analysis of science data from both the OASIS platforms and external sources such as satellite imagery and fixed sensors. These data are used by the SSA in planning vessel navigational trajectories for data gathering. The SSA also provides an operator interface for those occasions when a scientist desires to exert direct monitoring and control of individual platforms and their instruments.

Using this architecture, multiple mobile sensing assets can function in a cooperative fashion with the operating mode able to range from totally autonomous control to tele-operated control. This increases the data-gathering effectiveness and science return while reducing the demands on scientists for tasking, control, and monitoring. This system is applicable also to areas where multiple sensing assets are needed like ecological forecasting, water management, carbon management, disaster management, coastal management, homeland security, and planetary exploration.

This work was done by Gregg W. Podnar and John M. Dolan of Carnegie Mellon University, Alberto Elfes of Caltech, and Jeffrey C. Hosler and Troy J. Ames of Goddard Space Flight Center for NASA’s Jet Propulsion Laboratory. Further information is contained in a TSP (see page 1). NPO-45478



Synthesis of Submillimeter Radiation for Spectroscopy

A low-power, lightweight radiation source operates over a wide frequency range.

NASA's Jet Propulsion Laboratory, Pasadena, California

The frequency-multiplier submillimeter spectrometer (FMSS) is a laboratory apparatus for far-infrared molecular spectroscopy, embodying several advances over prior such apparatuses. The most innovative part of the FMSS is a source of monochromatic submillimeter-wavelength radiation that can be tuned over a wide frequency range, as needed for trace gas analyses and molecular-structure studies for which such apparatuses are typically used.

The radiation source features a modular design and is built mostly from commercially available components. It includes a computer-controlled radio-frequency synthesizer, amplifiers, and frequency multipliers of a type heretofore used in local oscillators for heterodyne far-infrared receivers. In conjunction with the rest of the apparatus, this source makes it possible to perform measurements over large portions of the submillimeter-wavelength spectrum with resolution, accuracy, and sensitivity greater than those achievable in Fourier-transform infrared spectroscopy. In comparison with prior laboratory sub-

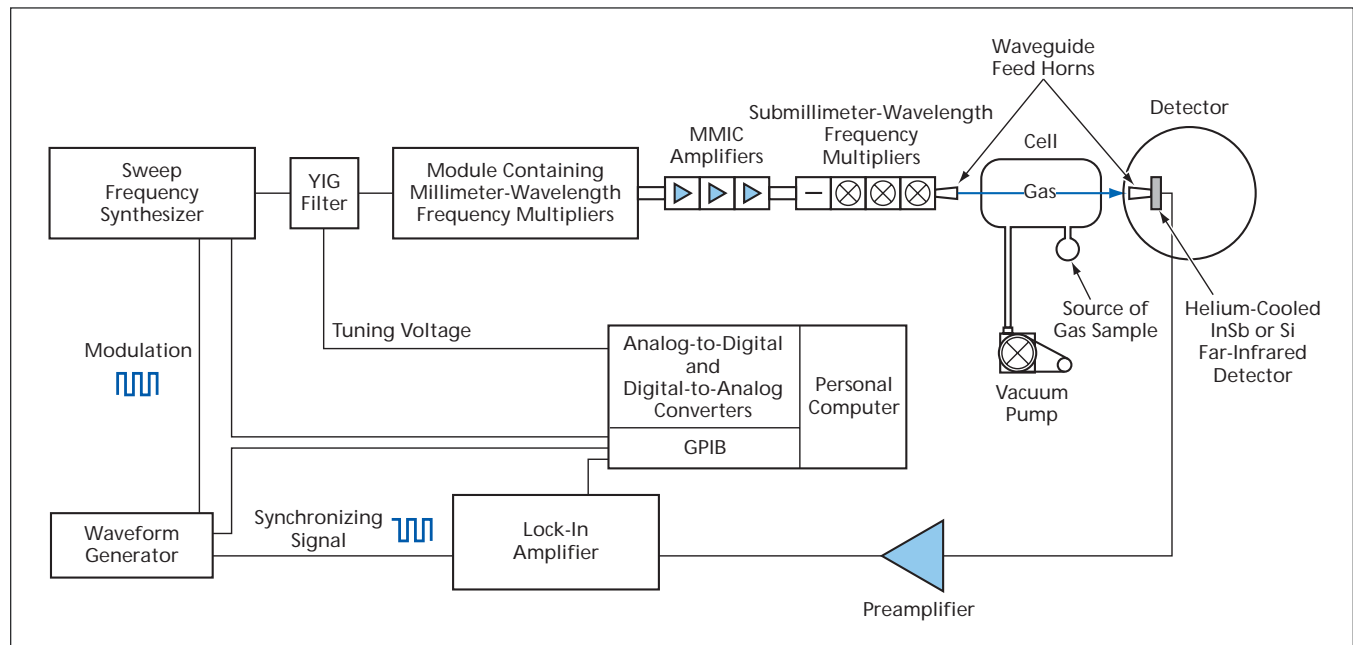
millimeter-wavelength radiation sources, this source is much lighter in weight, less cumbersome, less power-hungry, and capable of sustained operation with less intervention by laboratory personnel. Also, unlike some prior submillimeter-wavelength sources, this source does not require a high-voltage power source.

As shown in more detail in the figure, the radiation source includes a sweep frequency synthesizer connected to an external waveform generator, the output of which is used as a reference signal. The synthesizer is computer-controlled through a standard general-purpose interface bus (GPIB) and is operated in phase-locked continuous-wave mode for all measurements. The synthesizer output ranges in frequency from 11 to 18 GHz. For suppression of frequency spurs and harmonics, the output of the frequency synthesizer is fed through a tunable yttrium iron garnet (YIG) filter, which is swept in frequency simultaneously with the frequency synthesizer.

The output of the YIG filter is fed through a series of modular Schottky-

diode frequency multipliers and monolithic microwave integrated-circuit (MMIC) amplifiers that can be arranged in various combinations to obtain the desired submillimeter-wavelength radiation for spectroscopy, generally in the frequency range from 0.50 to 2.60 THz. By means of waveguide feed horns, the radiation is quasi-optically coupled through a cell containing a low-pressure gas to be analyzed. After passing through the cell, the radiation is detected by use of phase-sensitive electronic circuitry, and demodulated absorption signals are digitized and recorded in a computer. The absorption signals can subsequently be analyzed: for example, they can be compared with known absorption spectra in a database to determine the concentrations of molecular species of interest in the gas.

This work was done by Frank Maiwald, John Pearson, and Brian Drouin of Caltech for NASA's Jet Propulsion Laboratory. For further information, contact iaoffice@jpl.nasa.gov. NPO-43091



The Frequency-Multiplier Submillimeter Spectrometer is built around a radiation source that includes a computer-controlled radio-frequency synthesizer followed by a chain of multipliers and amplifiers that bring the output up to the 0.50-to-2.60-THz frequency range.

100-GHz Phase Switch/Mixer Containing a Slot-Line Transition

This circuit is compatible with MMICs.

NASA's Jet Propulsion Laboratory, Pasadena, California

A circuit that can function as a phase switch, frequency mixer, or frequency multiplier operates over a broad frequency range in the vicinity of 100 GHz. Among the most notable features of this circuit is a grounded uniplanar transition (in effect, a balun) between a slot line and one of two coplanar waveguides (CPWs). The design of this circuit is well suited to integration of the circuit into a microwave monolithic integrated circuit (MMIC) package.

One CPW is located at the input end and one at the output end of the top side of a substrate on which the circuit is fabricated (see Figure 1). The input CPW feeds the input signal to antiparallel flip-chip Schottky diodes connected to the edges of the slot line. Phase switching is effected by the combination of (1) the abrupt transition from the input CPW to the slot line and (2) CPW ground tuning effected by switching of the bias on the diodes.

Grounding of the slot metal to the bottom metal gives rise to a frequency cutoff in the slot. This cutoff is valuable for separating different frequency components when the circuit is used as a mixer or multiplier.

Proceeding along the slot line toward the output end, one encounters the aforementioned transition, which couples the slot line to the output CPW. Impedance tuning of the transition is accomplished by use of a high-impedance section immediately before the transition.

The uniplanarity of this transition is key to the utility of the circuit because it enables the top-side placement of all components [except via holes and the metal (ground plane) on the bottom side of the substrate], thereby making the circuit compatible with other circuits, components, and processes used to fabricate MMICs.

Figure 2 shows some results of tests of the circuit as a phase switch. Referring to the upper part of this figure, the pronounced increase in insertion loss at 91 GHz is attributed to a resonance of a substrate electromagnetic mode associated with the via holes. Subsequent modification of the via holes changed the frequency of (but did not eliminate) this resonance, making it possible to limit the insertion loss to approximately 5 dB over the frequency range from 90

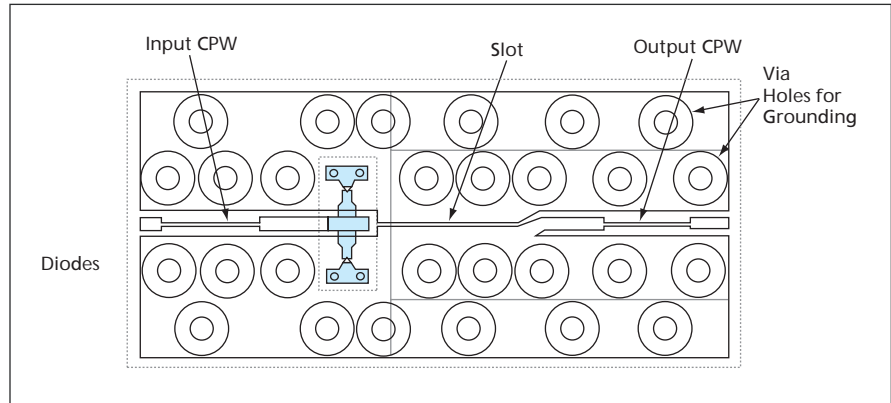


Figure 1. This Basic Layout of the Circuit shows the approximate locations of principal components mentioned in the text. Not shown here are wires crossing the CPWs that were added to provide inductive connections between top-metal grounds to suppress unwanted radiative electromagnetic modes.

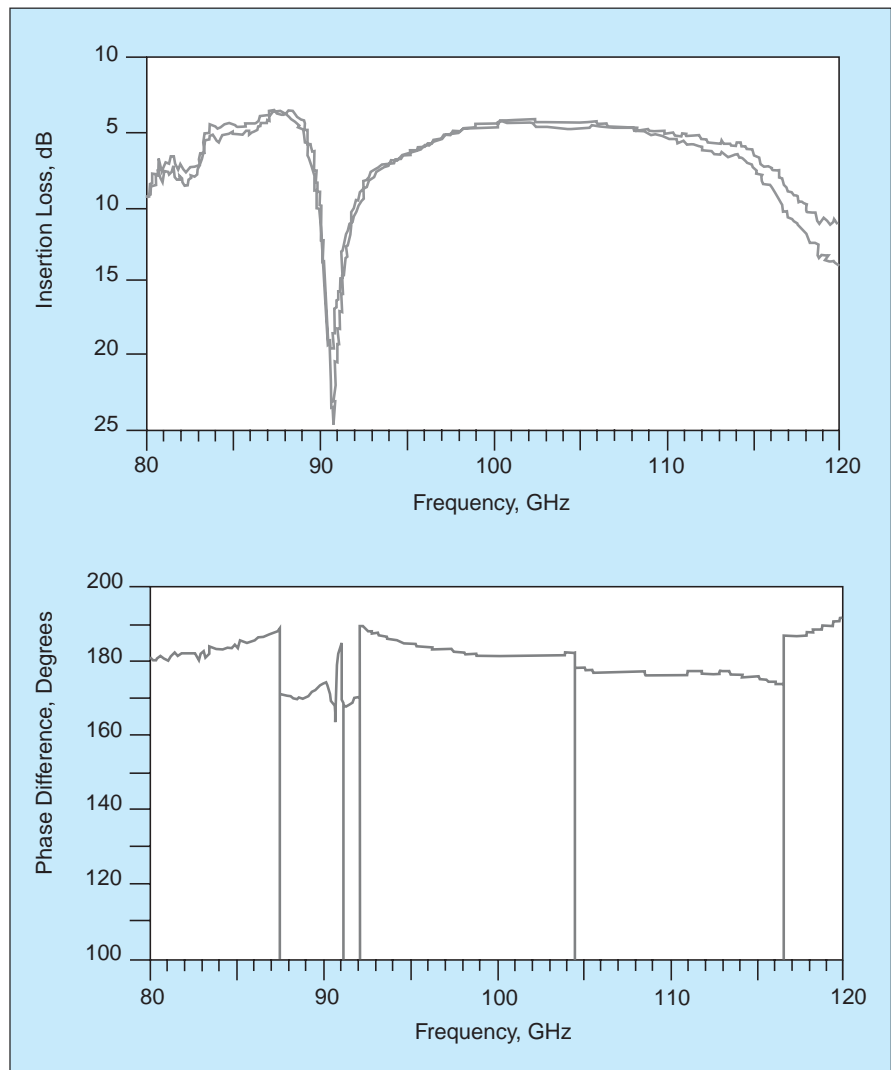


Figure 2. The Insertion Loss and Phase Difference introduced by the circuit operating as a phase switch were measured at frequencies from 80 to 120 GHz.

to 110 GHz. As shown in the lower part of Figure 2, the phase difference introduced by the switch remained within $\pm 10^\circ$ of the desired value of 180° over all but a small lower-edge portion of the frequency band from 90 to 110 GHz.

In a test of its performance as a balanced fundamental-frequency mixer, the circuit operated at a 12-dB conver-

sion loss, with an intermediate-frequency bandwidth of 25 GHz, at input frequencies from 78 to 110 GHz. This mixer performance is comparable to that of commercially available waveguide mixers, which, unlike this circuit, are not compatible with MMICs.

This work was done by Todd Gaier, Mary Wells, and Douglas Dawson of Cal-

tech for NASA's Jet Propulsion Laboratory.

This invention is owned by NASA, and a patent application has been filed. Inquiries concerning nonexclusive or exclusive license for its commercial development should be addressed to the Patent Counsel, NASA Management Office-JPL. For more information, contact iaoffice@jpl.nasa.gov. Refer to NPO-30916.

Generating Ka-Band Signals Using an X-Band Vector Modulator

Advanced modulations can be selected by programming an FPGA.

NASA's Jet Propulsion Laboratory, Pasadena, California

A breadboard version of a transmitter for radio communication at a carrier frequency of 32 GHz (which is in the Ka band) utilizes a vector modulator operating at a carrier frequency of 8 GHz (the low end of the X band) to generate any of a number of advanced modulations that could include amplitude and/or phase modulation components. The 8-GHz modulated signal is mixed with a 24-GHz signal generated by an up-converter to obtain the desired 32-GHz modulated output.

The transmitter is being developed as a prototype of downlink transmitters for transmission of data from spacecraft to Earth at high rates (>100 Mb/s). The transmitter design could also be adapted to terrestrial and Earth/satellite communication links. The advanced modulations (which can include *M*-ary phase-shift keying (*M*-PSK), offset phase-shift keying (OPSK), and *M*-ary quadrature amplitude modulation (*M*-QAM). These modulations are needed because for a given amount of signal bandwidth, they enable transmission of data at rates

greater than those of older, simpler modulation schemes.

The transmitter architecture (see figure) was chosen not only to enable generation of the required modulations at 32 GHz but also to reduce the number of components needed to implement the transmitter. Instead of incorporating an 8-GHz signal source, the transmitter utilizes an 8-GHz signal generated by a voltage-controlled oscillator that is part of an X-band transponder with which the fully developed version of this transmitter would be used in the original intended spacecraft application. The oscillator power is divided onto two paths, one of which goes through the vector modulator, the other through amplifiers and a $\times 3$ frequency multiplier. Band-pass filters are included downstream of the frequency multiplier to suppress unwanted harmonics.

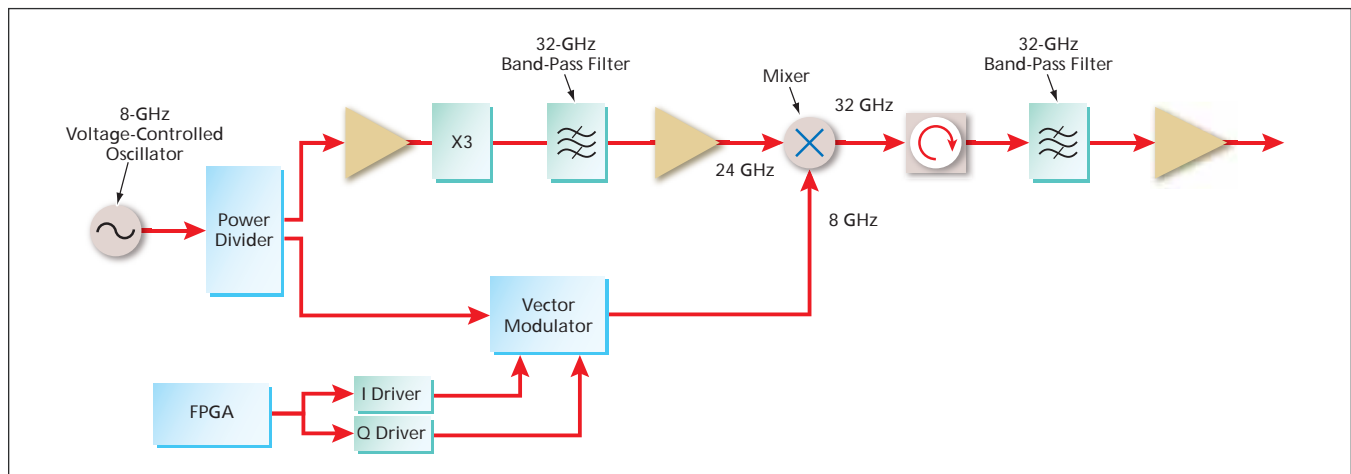
The in-phase (I) and quadrature (Q) components of the modulation are generated by use of a field-programmable gate array (FPGA) and fed through drivers to the vector modulator. The desired

modulation is selected or changed by programming the FPGA accordingly. Programming is controlled by use of an external computer connected to the FPGA via a universal serial bus.

The 24-GHz output of the frequency-multiplier path and the 8-GHz output of the modulator path are combined in a mixer to obtain the desired modulated 32-GHz signal. The performance of the mixer is improved by including an isolator in its output path. The isolator output is coupled through a 32-GHz band-pass filter to an output amplifier.

The transmitter performed well in initial tests, demonstrating capability for transmitting data at rates >100 Mb/s. In particular, data rates from 650 kb/s to 130 Mb/s were demonstrated using quadrature (quaternary) PSK and 16-QAM.

This work was done by Scott Smith, Narayan Mysoor, James Lux, Brian Cook, and Biren Shah of Caltech for NASA's Jet Propulsion Laboratory. For further information, contact iaoffice@jpl.nasa.gov. NPO-42995



To Obtain a 32-GHz Modulated Signal, an 8-GHz signal is multiplied in frequency to 24 GHz along one path and modulated along another path, then the outputs of the two paths are combined in a mixer.

SiC Optically Modulated Field-Effect Transistor

Such transistors could be useful as ultraviolet detectors.

John H. Glenn Research Center, Cleveland, Ohio

An optically modulated field-effect transistor (OFET) based on a silicon carbide junction field-effect transistor (JFET) is under study as, potentially, a prototype of devices that could be useful for detecting ultraviolet light. The SiC OFET is an experimental device that is one of several devices, including commercial and experimental photodiodes, that were initially evaluated as detectors of ultraviolet light from combustion and that could be incorporated into SiC integrated circuits to be designed to function as combustion sensors. The ultraviolet-detection sensitivity of the photodiodes was found to be less than desired, such that it would be necessary to process their outputs using high-gain amplification circuitry. On the other hand, in principle, the function of the OFET could be characterized as a combination of detection and amplification. In effect, its sensitivity

could be considerably greater than that of a photodiode, such that the need for amplification external to the photodetector could be reduced or eliminated.

The experimental SiC OFET was made by processes similar to JFET-fabrication processes developed at Glenn Research Center. The gate of the OFET is very long, wide, and thin, relative to the gates of typical prior SiC JFETs. Unlike in prior SiC FETs, the gate is almost completely transparent to near-ultraviolet and visible light. More specifically:

- The OFET includes a p⁺ gate layer less than 1/4 μm thick, through which photons can be transported efficiently to the p⁺/p body interface.
- The gate is relatively long and wide (about 0.5 by 0.5 mm), such that holes generated at the body interface form a depletion layer that modulates the conductivity of the channel between the drain and the source.

The exact physical mechanism of modulation of conductivity is a subject of continuing research. It is known that injection of minority charge carriers (in this case, holes) at the interface exerts a strong effect on the channel, resulting in amplification of the photon-detection signal. A family of operating curves characterizing the OFET can be generated in a series of measurements performed at different intensities of incident ultraviolet light.

This work was done by Massood Tabib-Azar of Case Western Reserve University for Glenn Research Center. Further information is contained in a TSP (see page 1).

Inquiries concerning rights for the commercial use of this invention should be addressed to NASA Glenn Research Center, Innovative Partnerships Office, Attn: Steve Fedor, Mail Stop 4-8, 21000 Brookpark Road, Cleveland, Ohio 44135. Refer to LEW-18349-1

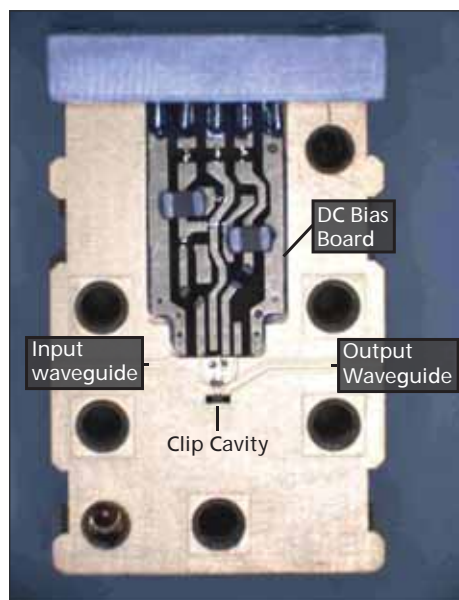
Submillimeter-Wave Amplifier Module With Integrated Waveguide Transitions

This technique can be used in submillimeter-wave imaging in homeland security, weapons detection, and commercial test equipment.

NASA's Jet Propulsion Laboratory, Pasadena, California

To increase the usefulness of monolithic millimeter-wave integrated circuit (MMIC) components at submillimeter-wave frequencies, a chip has been designed that incorporates two integrated, radial E-plane probes with an MMIC amplifier in between, thus creating a fully integrated waveguide module. The integrated amplifier chip has been fabricated in 35-nm gate length InP high-electron-mobility-transistor (HEMT) technology. The radial probes were mated to grounded coplanar waveguide input and output lines in the internal amplifier. The total length of the internal HEMT amplifier is 550 μm, while the total integrated chip length is 1,085 μm. The chip thickness is 50 μm with the chip width being 320 μm.

The internal MMIC amplifier is biased through wire-bond connections to the gates and drains of the chip. The chip has 3 stages, employing 35-nm gate length transistors in each



A photograph of the Split-Block Module, showing the input and output waveguide, chip cavity, and DC bias board.

stage. Wire bonds from the DC drain and gate pads are connected to off-chip shunt 51-pF capacitors, and additional off-chip capacitors and resistors are added to the gate and drain bias lines for low-frequency stability of the amplifier. Additionally, bond wires to the grounded coplanar waveguide pads at the RF input and output of the internal amplifier are added to ensure good ground connections to the waveguide package.

The S-parameters of the module, not corrected for input or output waveguide loss, are measured at the waveguide flange edges. The amplifier module has over 10 dB of gain from 290 to 330 GHz, with a peak gain of over 14 dB at 307 GHz. The WR2.2 waveguide cutoff is again observed at 268 GHz. The module is biased at a drain current of 27 mA, a drain voltage of 1.24 V, and a gate voltage of +0.21 V. Return loss of the module is very good between 5 to

25 dB. This result illustrates the usefulness of the integrated radial probe transition, and the wide (over 10-percent) bandwidth that one can expect for amplifier modules with integrated radial probes in the submillimeter-regime (>300 GHz).

This technology was developed for a submillimeter-wave imaging system under the DARPA SWIFT program, in collaboration with Northrop Grumman Corporation. Submillimeter-wave imaging has many applications to

homeland security, hidden weapons detection, airport security, detection of bio-weapons, as well as potential applications in commercial test equipment. This technology is partially a semiconductor chip product and partially a waveguide module. The semiconductor is not fixed in its final form, but the module is essentially fixed in its final form.

This work was done by Lorene Samoska, Goutam Chattopadhyay, David Pukala, Todd Gaier, Mary Soria, and King Man

Fung of Caltech and William Deal, Gerry Mei, Vesna Radisic, and Richard Lai of Northrop Grumman Corporation for NASA's Jet Propulsion Laboratory. The contributors would like to acknowledge the support of Dr. Mark Rosker and the Army Research Laboratory. This work was supported by the DARPA SWIFT Program and Army Research Laboratory under the DARPA MIPR no. 06-U037 and ARL Contract no. W911QX-06-C-0050. Further information is contained in a TSP (see page 1). NPO-45088

Metrology System for a Large, Somewhat Flexible Telescope

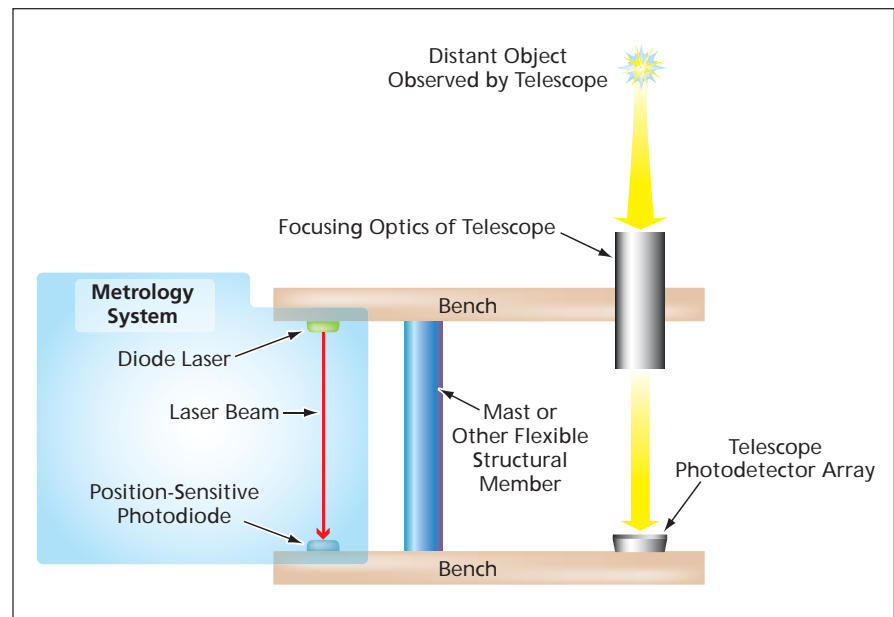
This system would measure focal-plane position errors caused by structural deformations.

NASA's Jet Propulsion Laboratory, Pasadena, California

A proposed metrology system would be incorporated into a proposed telescope that would include focusing optics on a rigid bench connected via a deployable mast to another rigid bench holding a focal-plane array of photon counting photodetectors. Deformations of the deployable mast would give rise to optical misalignments that would alter the directions (and, hence, locations) of incidence of photons on the focal plane. The metrology system would measure the relative displacement of the focusing-optics bench and the focal-plane array bench. The measurement data would be used in post-processing of the digitized photodetector outputs to compensate for the mast-deformation-induced changes in the locations of incidence of photons on the focal plane, thereby making it possible to determine the original directions of incidence of photons with greater accuracy.

The proposed metrology system is designed specifically for the Nuclear Spectroscopic Telescope Array (NuSTAR) a proposed spaceborne x-ray telescope. The basic principles of design and operation are also applicable to other large, somewhat flexible telescopes, both terrestrial and spaceborne. In the NuSTAR, the structural member connecting the optical bench and the photodetector array would be a 10-m-long deployable mast, and there is a requirement to keep errors in measured directions of incidence of photons below 10 arc seconds (3 sigma).

The proposed system would include three diode lasers that would be mounted on the focusing-optics bench. For clarity, only one laser is



This Deformation of the Mast would change the position of incidence of the laser beam on the position-sensitive photodiode.

shown in the figure, which is a greatly simplified schematic diagram of the system. Each laser would be aimed at a position-sensitive photodiode that would be mounted on the detector bench alongside the aforementioned telescope photodetector array. The diode lasers would operate at a wavelength of 830 nm, each at a power of 200 mW. Each laser beam would be focused to a spot of ≈ 1 -mm diameter on the corresponding position-sensitive photodiode. To reduce the effect of sunlight on the measurements, a one-stage light baffle and an 830-nm transmission filter of 10-nm bandwidth would be placed in front of the posi-

tion-sensitive photodiode. For each metrology reading, the output of the position-sensitive detector would be sampled and digitized twice: once with the lasers turned on, then once with the lasers turned off. The data from these two sets of samples would be subtracted from each other to further reduce the effects of sun glints or other background light sources.

This work was done by Carl Christian Liebe, Randall Bartman, and Walter Cook of Caltech and William Craig of Lawrence Livermore National Laboratory for NASA's Jet Propulsion Laboratory. Further information is contained in a TSP (see page 1). NPO-44119

Economical Implementation of a Filter Engine in an FPGA

There are numerous potential uses in general signal processing.

NASA's Jet Propulsion Laboratory, Pasadena, California

A logic design has been conceived for a field-programmable gate array (FPGA) that would implement a complex system of multiple digital state-space filters. The main innovative aspect of this design lies in providing for reuse of parts of the FPGA hardware to perform different parts of the filter computations at different times, in such a manner as to enable the timely performance of all required computations in the face of limitations on available FPGA hardware resources.

A digital state-space filter of the type to which the design applies (see figure) is represented by the equations

$$\mathbf{x}(k+1) = \mathbf{A}\mathbf{x}(k) + \mathbf{B}u(k) \quad (1)$$

and

$$y(k) = \mathbf{C}\mathbf{x}(k) + Du(k) \quad (2)$$

where:

k is an integer representing an increment of time,

N is an integer representing the number of dimensions in the state space,

$u(k)$ is a scalar input at time k ,

$y(k)$ is a scalar output at time k ,

$\mathbf{x}(k)$ is an $N \times 1$ state vector at time k ,

\mathbf{A} is an $N \times N$ matrix of filter coefficients,

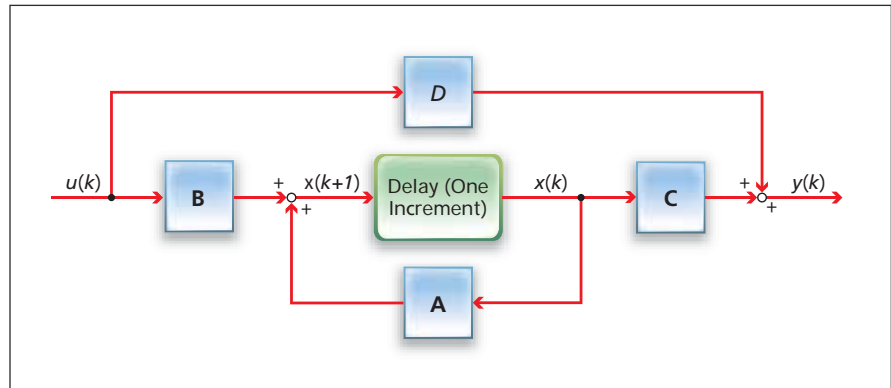
\mathbf{B} is an $N \times 1$ vector of filter coefficients,

\mathbf{C} is a $1 \times N$ vector of filter coefficients, and

D is a scalar filter coefficient.

The implementation of the digital state-space filter involves matrix-vector multiplications, which, in the absence of the present innovation, would ordinarily necessitate some multiplexing of vector elements and/or routing of data flows along multiple paths.

The design concept calls for implementing vector registers as shift registers



This Block Diagram represents a digital state-space filter, which could be one of multiple such filters in a complex system. The same FPGA circuitry could be used to implement different filters at different times.

to simplify operand access to multipliers and accumulators, obviating both multiplexing and routing of data along multiple paths. Each vector register would be reused for different parts of a calculation. Outputs would always be drawn from the same register, and inputs would always be loaded into the same register.

A simple state machine would control each filter. The output of a given filter would be passed to the next filter, accompanied by a "valid" signal, which would start the state machine of the next filter. Multiple filter modules would share a multiplication/accumulation arithmetic unit. The filter computations would be timed by use of a clock having a frequency high enough, relative to the input and output data rate, to provide enough cycles for matrix and vector arithmetic operations.

This design concept could prove beneficial in numerous applications in which digital filters are used and/or vectors are multiplied by coefficient matrices. Examples of such applications include general signal processing, filtering of signals in control systems, processing of geophysical measurements, and medical imaging. For these and other applications, it could be advantageous to combine compact FPGA digital filter implementations with other application-specific logic implementations on single integrated-circuit chips. An FPGA could readily be tailored to implement a variety of filters because the filter coefficients would be loaded into memory at startup.

This work was done by James E. Kowalski of Caltech for NASA's Jet Propulsion Laboratory. Further information is contained in a TSP (see page 1). NPO-44662.



Improved Joining of Metal Components to Composite Structures

Uncured composite material is intertwined with metal studs, then cured.

Marshall Space Flight Center, Alabama

Systems requirements for complex spacecraft drive design requirements that lead to structures, components, and/or enclosures of a multi-material and multifunctional design. The varying physical properties of aluminum, tung-

sten, Invar, or other high-grade aerospace metals when utilized in conjunction with lightweight composites multiply system level solutions. These multi-material designs are largely dependent upon effective joining tech-

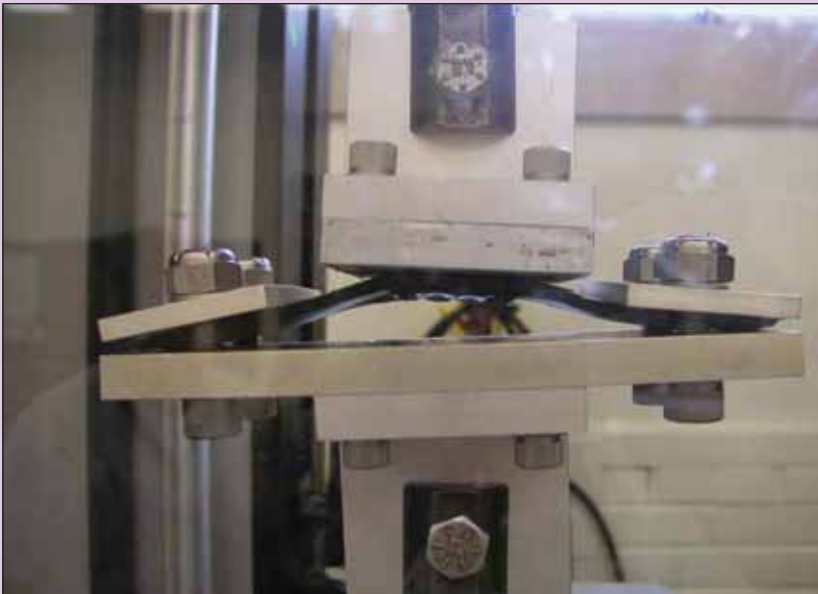
niques, which create a “monolithic,” well-integrated and seamlessly functional structure.

An improved method of joining metal components to matrix/fiber composite-material structures has been invented. The method is particularly applicable to equipping such thin-wall polymer-matrix composite (PMC) structures as tanks with flanges, ceramic matrix composite (CMC) liners for high heat engine nozzles, and other metallic-to-composite attachments. The method is oriented toward new architectures and distributing mechanical loads as widely as possible in the vicinities of attachment locations to prevent excessive concentrations of stresses that could give rise to delaminations, debonds, leaks, and other failures.

The method in its most basic form can be summarized as follows: A metal component is to be joined to a designated attachment area on a composite-material structure. In preparation for joining, the metal component is fabricated to include multiple “studs” projecting from the aforementioned face. Also in preparation for joining, holes just wide enough to accept the studs are molded into, drilled, or otherwise formed in the corresponding locations in the designated attachment area of the uncured (“wet”) composite structure. The metal component is brought together with the uncured composite structure so that the studs become firmly seated in the holes, thereby causing the composite material to become intertwined with the metal component in the joining area. Alternately, it is proposed to utilize other mechanical attachment schemes whereby the uncured composite and metallic parts are joined with “z-direction” fasteners. The resulting “wet” assembly is then subjected to the composite-curing heat treatment, becoming a unitary structure. It should be noted that this new art will require different techniques for CMC’s versus PMC’s, but the final architecture and companion curing philosophy is the same. For instance, a chemical vapor infiltration (CVI) fabrication technique may require special integration of the pre-form and



UNCURED COMPOSITE PLATE JOINED TO ALUMINUM PLATE WITH SCREWS



CURED COMPOSITE/ALUMINUM STRUCTURE IN TENSILE TESTING MACHINE AT END OF TEST

A Composite/Metal Joint of the type described in the text was fabricated, then subjected to a tensile/bending test.

metallic part, as well as, high-temperature metals or transitional molten metals to achieve the desired architecture.

The method accommodates numerous variations. For example, in a demonstration of the method, an aluminum plate having dimensions of 4 by 3 by 0.50 in. (about 10.2 by 7.6 by 1.3 cm) was joined with a 2-by-8-by-0.25-in. (about 5.1-by-20.3-by-0.6-cm) plate made of composite of carbon fibers in an epoxy (thermoset) matrix toughened with a thermoplastic material. The composite plate was prepared in uncured form, and 16 holes were predrilled in the aluminum plate to accept thread-tapping screws intended to serve as substitutes

for studs. The array of these holes was used as a template to drill 16 corresponding holes in the uncured composite plate. The screws were inserted through the holes in the uncured composite plate and tightened into the holes in the aluminum plate (see upper part of figure). The resulting assembly was placed in an autoclave, where it was heated to a temperature of 350 °F (≈177 °C) to cure the epoxy. Then the assembly was cooled very slowly [between 10 and 15 °F (between about 5.6 and 8.3 °C) per hour] so that the difference between the coefficients of thermal expansion of the aluminum and the composite would not induce excessive stress.

The resulting unitary structure was subjected to a tensile/bending test as shown in the lower part of the figure. When the test was terminated at a load of 4,683 lb (≈20.8 kN), the composite panel was bent significantly, but no sign of failure of the joint was visible. [The screws were rated to withstand a load of 10,240 lb (≈45.5 kN).]

This work was done by Edmund Semmes of Marshall Space Flight Center.

This invention is owned by NASA, and a patent application has been filed. For further information, contact Sammy Nabors, MSFC Commercialization Assistance Lead, at sammy.a.nabors@nasa.gov. Refer to MFS-31813-1.

Machined Titanium Heat-Pipe Wick Structure

Wicks are fabricated separately, then inserted in tubes.

John H. Glenn Research Center, Cleveland, Ohio

Wick structures fabricated by machining of titanium porous material are essential components of lightweight titanium/water heat pipes of a type now being developed for operation at temperatures up to 530 K in high-radiation environments. In the fabrication of some prior heat pipes, wicks have been made by extruding axial grooves into aluminum — unfortunately, titanium

cannot be extruded. In the fabrication of some other prior heat pipes, wicks have been made by *in-situ* sintering of metal powders shaped by the use of forming mandrels that are subsequently removed, but in the specific application that gave rise to the present fabrication method, the required dimensions and shapes of the heat-pipe structures would make it very difficult if not impossible to

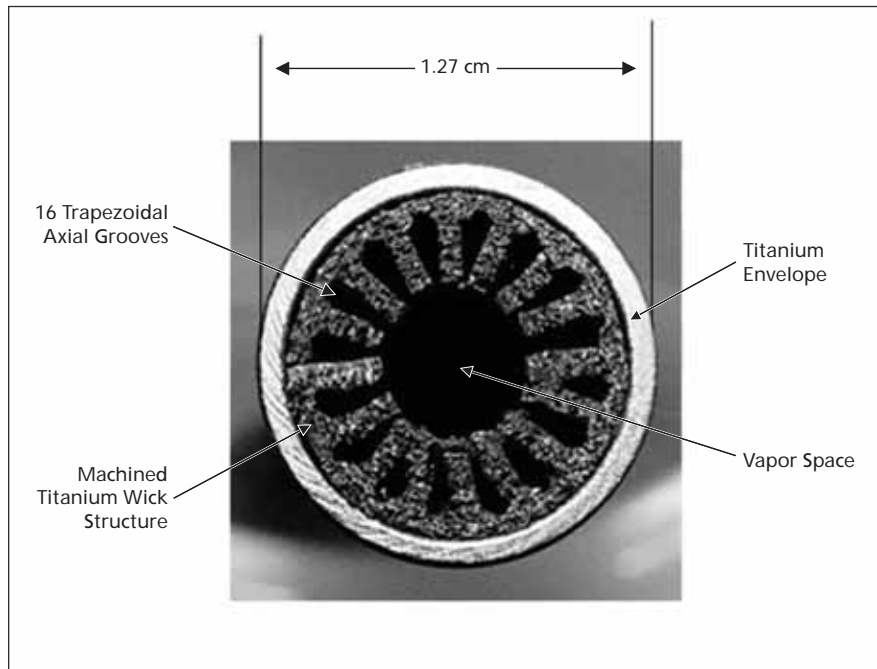
remove the mandrels due to the length and the small diameter.

In the present method, a wick is made from one or more sections that are fabricated separately and assembled outside the tube that constitutes the outer heat-pipe wall. The starting wick material is a slab of porous titanium material. This material is machined in its original flat configuration to form axial grooves. In addition, interlocking features are machined at the mating ends of short wick sections that are to be assembled to make a full-length continuous wick structure. Once the sections have been thus assembled, the resulting full-length flat wick structure is rolled into a cylindrical shape and inserted in the heat-pipe tube (see figure).

This wick-structure fabrication method is not limited to titanium/water heat pipes: It could be extended to other heat pipe materials and working fluids in which the wicks could be made from materials that could be pre-formed into porous slabs.

This work was done by John H. Rosenfeld, Kenneth G. Minnerly, and Nelson J. Gernert of Thermacore Inc. for Glenn Research Center.

Inquiries concerning rights for the commercial use of this invention should be addressed to NASA Glenn Research Center, Innovative Partnerships Office, Attn: Steve Fedor, Mail Stop 4-8, 21000 Brookpark Road, Cleveland, Ohio 44135. Refer to LEW-18206-1.



Machined Titanium Heat Pipe Wick Structure is shown in cross section.



Gadolinia-Doped Ceria Cathodes for Electrolysis of CO₂

These electrodes have relatively low area-specific resistances.

John H. Glenn Research Center, Cleveland, Ohio

Gadolinia-doped ceria, or GDC, ($Gd_{0.4}Ce_{0.6}O_{2-\delta}$, where the value of δ in this material varies, depending on the temperature and oxygen concentration in the atmosphere in which it is being used) has shown promise as a cathode material for high-temperature electrolysis of carbon dioxide in solid oxide electrolysis cells. The polarization resistance of a GDC electrode is significantly less than that of an otherwise equivalent electrode made of any of several other materials that are now in use or under consideration for use as cathodes for reduction of carbon dioxide. In addition, GDC shows no sign of deterioration under typical temperature and gas-mixture operating conditions of a high-temperature electrolyzer.

Electrolysis of CO₂ is of interest to NASA as a way of generating O₂ from the CO₂ in the Martian atmosphere. On Earth, a combination of electrolysis of CO₂ and electrolysis of H₂O might prove useful as a means of generating synthesis gas (“syngas”) from the exhaust gas of a coal- or natural-gas-fired power plant, thereby reducing the emission of CO₂ into the atmosphere. The syngas — a mixture of CO and H₂ — could be used as a raw material in the manufacture, via the Fisher-Tropsch process, of synthetic fuels, lubrication oils, and other hydrocarbon products.

An electrolysis cell of the type of interest here consists of a solid oxide electrolyte coated on each side with a porous electrode (see Figure 1). A suitable electric potential is applied to the electrodes, causing electrolysis of CO₂ to proceed via overall reaction $CO_2 \rightarrow CO + O$. At the cathode, carbon dioxide is reduced to carbon monoxide and negative oxygen ions in the half-cell reaction $CO_2 + 2e^- \rightarrow CO + O^{2-}$. The carbon monoxide leaves the cell in the carbon dioxide stream. The solid oxide electrolyte conducts the O²⁻ ions (that is to say, the O²⁻ ions diffuse across the solid oxide electrolyte). Upon reaching the anode, the oxygen ions combine to

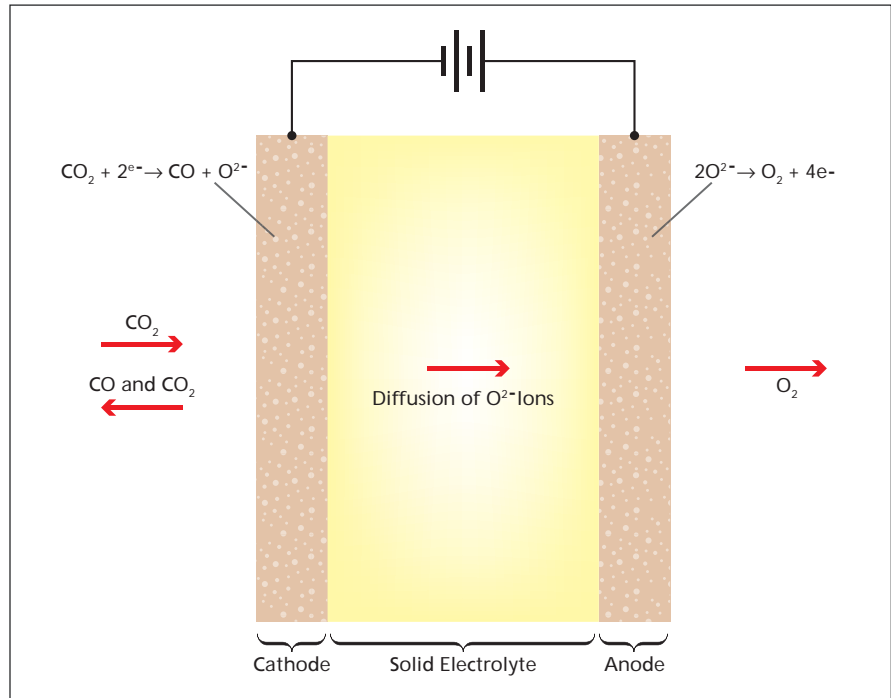


Figure 1. This Schematic Diagram depicts the basic operation of a solid-oxide CO₂-electrolyzer cell.

form oxygen molecules, the overall half-cell reaction sequence being $2O^{2-} \rightarrow 2e^- + O_2$. If the solid oxide electrolyte is made of yttria-stabilized zirconia (YSZ), then it conducts only oxygen ions (but not CO₂ or CO), so that essentially pure oxygen is produced on the anode side.

This process is energy-intensive: The enthalpy of the overall reaction is positive and very large (+283 kJ/mole) — comparable to the enthalpy for the electrolysis of water

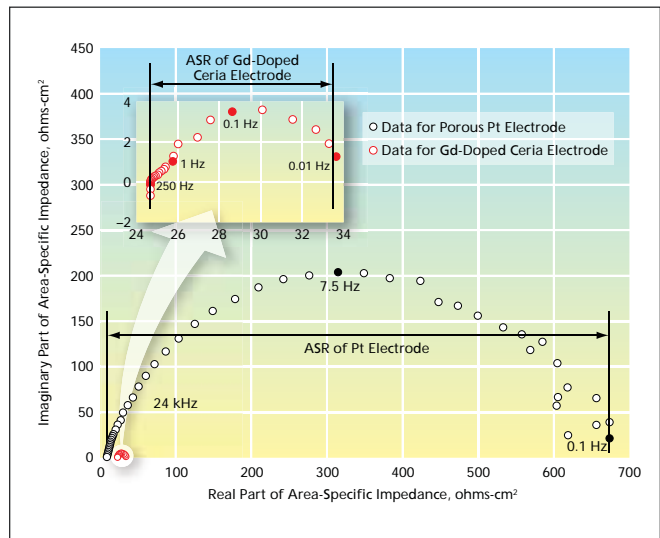


Figure 2. A Nyquist Plot of the AC Impedance Spectra for a GDC and porous Pt electrodes shows measured results on symmetric cells under zero-bias voltage conditions. The measurements were made during operation of the cells at a temperature of 800 °C in a mixture of 5 mole percent of CO and 95 mole percent of CO₂ at a pressure of 1 atm (=0.1 MPa). The ASR of each electrode is the difference between the intersections of its spectral plot with the real axis.

(+286 kJ/mole). In order to make this process economically viable, it is necessary to minimize any irreversible energy losses, notably including those associated with overpotentials and ohmic resistances.

In most of the previous work on electrolysis of CO₂ in cells containing YSZ solid electrolytes, both the cathodes and the anodes have been made of porous Pt. The choice of GDC as the present candidate cathode material was prompted by several considerations:

- GDC is much less expensive (about \$1,200 per kilogram of GDC versus about \$39,000 per kilogram of Pt at 2005 market prices).
- Ceria is known to enhance oxidation of CO when used as a catalyst support in automobile catalytic converters.
- Ceria appears to be an effective an electrocatalyst for oxidation of CO/H₂ mixtures and low molecular weight hydrocarbons (methane) in solid oxide fuel cells.
- GDC acts as a mixed conductor: it conducts both ions and electrons, enabling CO₂-reduction reactions to occur over a larger electrode area and volume than would otherwise be avail-

able for such reactions, thereby reducing the polarization resistance below that of a comparable electrode made of a different material.

Therefore, the performance of GDC as a candidate cathode material, in comparison with the performance of porous Pt as a cathode material, was investigated via electrochemical measurements on symmetric GDC/YSZ/GDC cells and compared with similar measurements on a symmetric Pt/YSZ/Pt cell. Each GDC/YSZ/GDC cell was fabricated by brushing a GDC/organic-binder mixture onto both faces of a thick cylindrical YSZ pellet, then sintering the cell at a temperature of 1,250 °C. The experiments involved several different CO/CO₂ mixtures and temperatures from 700 to 950 °C. In the experiments, electrochemical impedance spectroscopy (EIS) was performed. Area-specific resistance (ASR) values were calculated from the EIS measurements. The ASR values for the cells containing GDC electrodes were found to be substantially lower than that of the cell containing Pt electrodes under identical test conditions, as shown in Figure 2. Lower ASR values are expected to translate to lower

overpotentials and, hence, lower power consumption in electrolyzers.

On the basis of limited published data, it appears that the ASRs of GDC electrodes may also be lower than those of electrodes made of Ni-YSZ, a cermet electrode material commonly used in anodes of state-of-the-art solid-oxide fuel cells. Testing of one of the cells containing GDC electrodes was continued for more than 300 hours, and no degradation of performance was observed; on the contrary, the ASR decreased slightly during the test. In addition, there was no sign of coking (deposition of carbon), which is known to occur in other electrode materials under the gas-mixture and temperature conditions used in the tests.

This work was done by Robert D. Green of Glenn Research Center and Stuart B. Adler of the University of Washington. Further information is contained in a TSP (see page 1).

Inquiries concerning rights for the commercial use of this invention should be addressed to NASA Glenn Research Center, Innovative Partnerships Office, Attn: Steve Fedor, Mail Stop 4-8, 21000 Brookpark Road, Cleveland, Ohio 44135. Refer to LEW-18211-1.



Utilizing Ocean Thermal Energy in a Submarine Robot

An OTEC thermodynamic cycle would be divided into surface and depth phases.

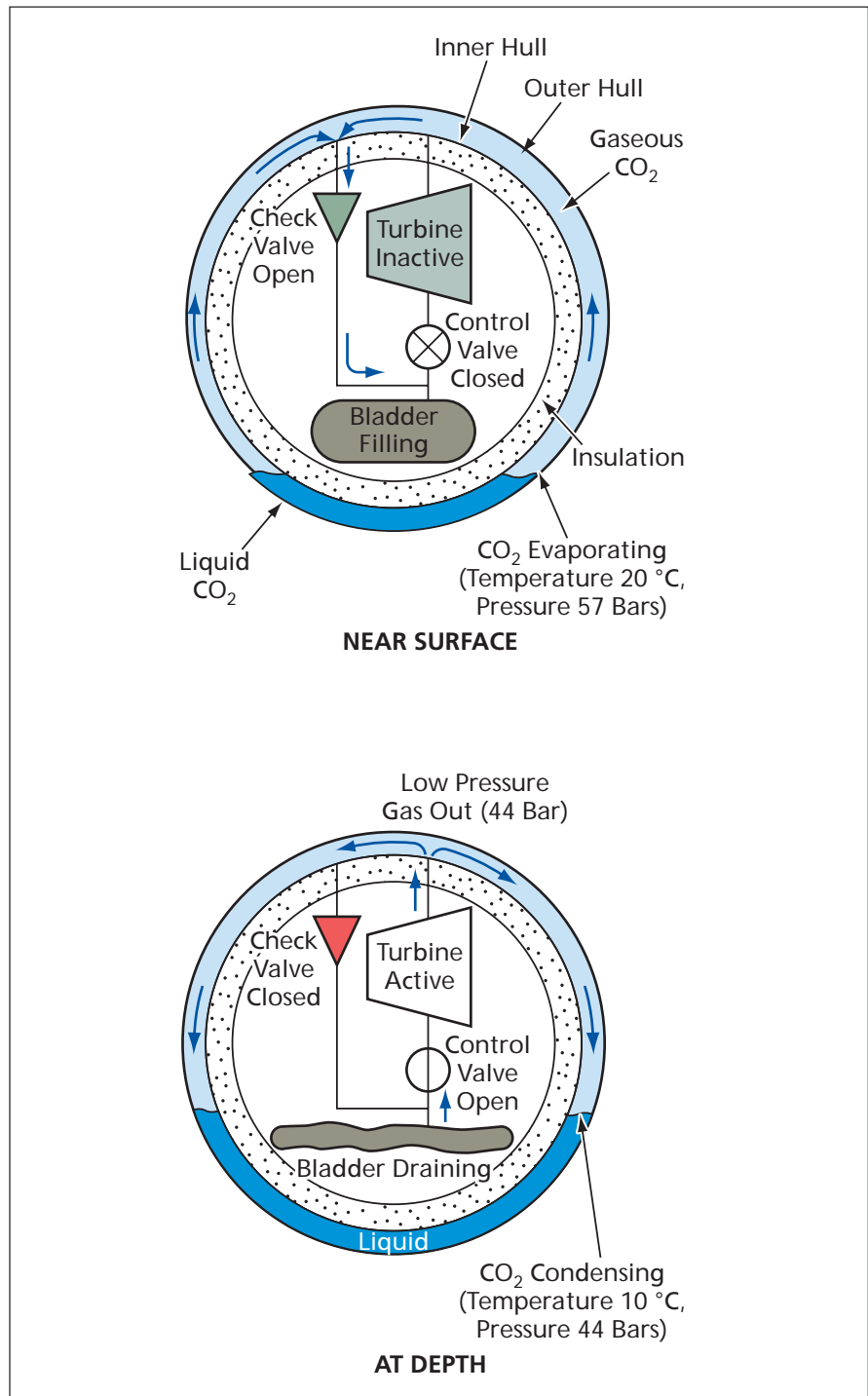
NASA's Jet Propulsion Laboratory, Pasadena, California

A proposed system would exploit the ocean thermal gradient for recharging the batteries in a battery-powered unmanned underwater vehicle [UUV (essentially, a small exploratory submarine robot)] of a type that has been deployed in large numbers in research pertaining to global warming. A UUV of this type travels between the ocean surface and depths, measuring temperature and salinity. The proposed system is related to, but not the same as, previously reported ocean thermal energy conversion (OTEC) systems that exploit the ocean thermal gradient but consist of stationary apparatuses that span large depth ranges.

The system would include a turbine driven by working fluid subjected to a thermodynamic cycle. CO₂ has been provisionally chosen as the working fluid because it has the requisite physical properties for use in the range of temperatures expected to be encountered in operation, is not flammable, and is much less toxic than are many other commercially available refrigerant fluids. The system would be housed in a pressurized central compartment in a UUV equipped with a double hull (see figure).

The thermodynamic cycle would begin when the UUV was at maximum depth, where some of the CO₂ would condense and be stored, at relatively low temperature and pressure, in the annular volume between the inner and outer hulls. The cycle would resume once the UUV had ascended to near the surface, where the ocean temperature is typically ≥ 20 °C. At this temperature, the CO₂ previously stored at depth in the annular volume between the inner and outer hulls would be pressurized to ≈ 57 bar (5.7 MPa). The pressurized gaseous CO₂ would flow through a check valve into a bladder inside the pressurized compartment, thereby storing energy of the relatively warm, pressurized CO₂ for subsequent use after the next descent to maximum depth.

Upon descent, the outer hull would become cooled — possibly to a minimum



CO₂ Would Be Pressurized by heating near the ocean surface. Later, at depth, pressurized CO₂ would be allowed to expand through the turbine and condensed at lower temperature.

temperature as low as about 4 °C at a depth of about 300 m. The cooling would reduce the pressure of the CO₂ remaining in the annular volume to about 44 bars (4.4 MPa) or less. Then a control valve would be opened, allowing CO₂

from the pressurized bladder to expand through a turbine, thus producing electricity for recharging the battery. After flowing through the turbine and the control valve, the CO₂ would enter the annular volume, where it would be condensed

at low temperature and pressure, completing the thermodynamic cycle.

This work was done by Jack Jones and Yi Chao of Caltech for NASA's Jet Propulsion Laboratory. Further information is contained in a TSP (see page 1). NPO-43304

⚙️ Fuel-Cell Power Systems Incorporating Mg-Based H₂ Generators

Hydrogen would be generated from magnesium and steam.

NASA's Jet Propulsion Laboratory, Pasadena, California

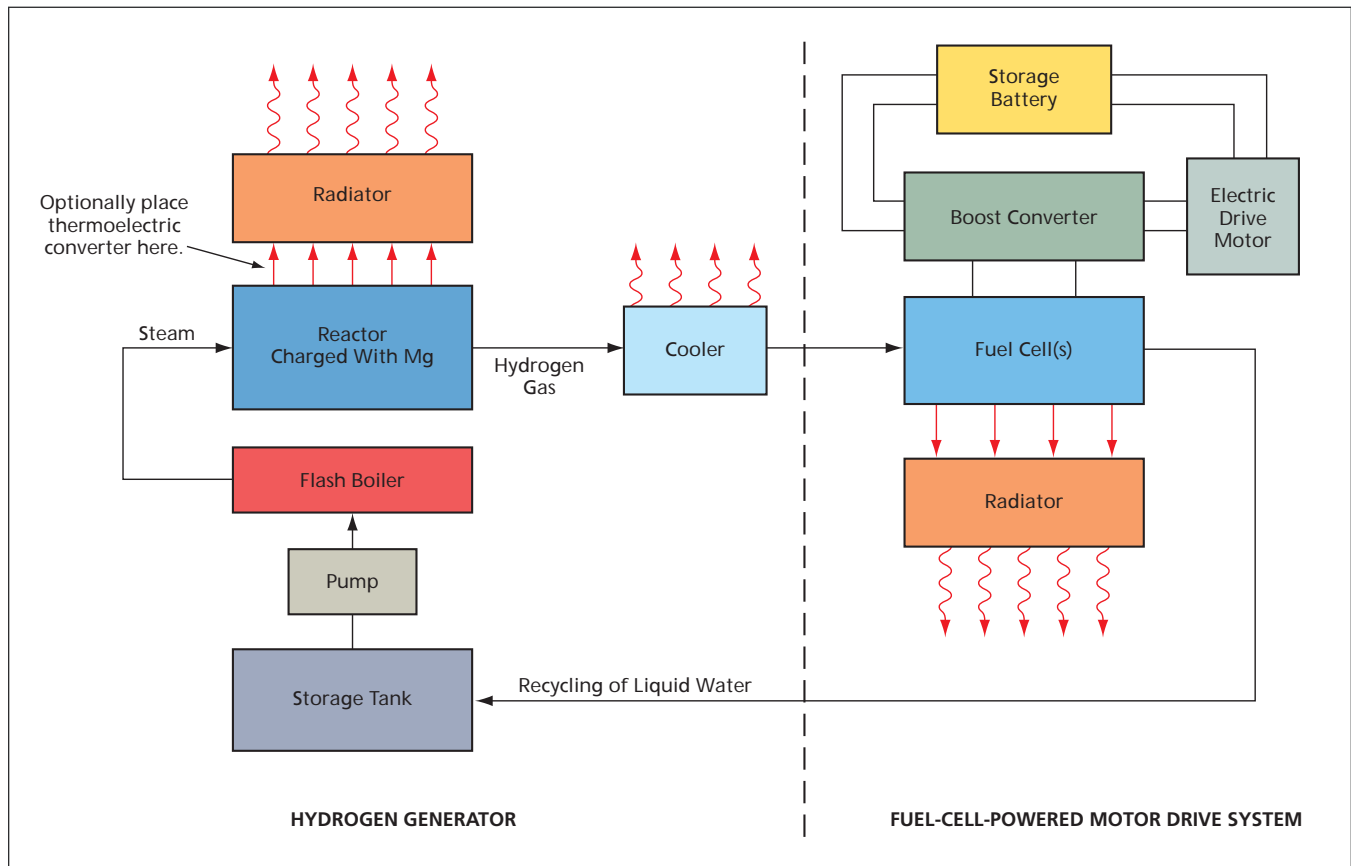
Two hydrogen generators based on reactions involving magnesium and steam have been proposed as means for generating the fuel (hydrogen gas) for such fuel-cell power systems as those to be used in the drive systems of advanced motor vehicles. The hydrogen generators would make it unnecessary to rely on any of the hydrogen-storage systems developed thus far that are, variously, too expensive, too heavy, too bulky, and/or too unsafe to be practical.

The two proposed hydrogen generators are denoted basic and advanced, respectively. In the basic hydrogen generator (see figure), steam at a temperature

≥330 °C would be fed into a reactor charged with magnesium, wherein hydrogen would be released in the exothermic reaction $Mg + H_2O \rightarrow MgO + H_2$. The steam would be made in a flash boiler. To initiate the reaction, the boiler could be heated electrically by energy borrowed from a storage battery that would be recharged during normal operation of the associated fuel-cell subsystem. Once the reaction was underway, heat from the reaction would be fed to the boiler. If the boiler were made an integral part of the hydrogen-generator reactor vessel, then the problem of transfer of heat from the reactor to the boiler would be greatly simplified. A pump

would be used to feed water from a storage tank to the boiler.

Only a small fraction of the heat generated in the reaction would be needed for boiling: For every kilogram of hydrogen produced, about 44.5 kW·h of heat would be generated, while only about 6 kW·h would be needed to boil the requisite amount of water. The remaining 38.5 kW·h of high-grade heat would have to be dissipated via a radiator. Optionally, the flow of heat from the reactor to the radiator could be intercepted by a thermoelectric converter, thereby increasing the overall electric power generated; the net increase in the overall efficiency of the fuel-cell power system has



The Basic Hydrogen Generator is shown here as feeding hydrogen gas as fuel to a fuel-cell-powered motor drive system

been estimated to be equivalent to that afforded by an increase of 19 percent in the amount of hydrogen generated.

The generated hydrogen would be sent through a cooler to reduce its temperature to 80 °C as required for the fuel cell(s). During operation of a hydrogen-burning fuel cell, water is generated in liquid and vapor forms. The liquid water could easily be recycled to the storage tank. Depending on detailed calculations yet to be performed, it may be advantageous to also recycle the water vapor by condensing it and pumping the resulting liquid water to the storage tank, provided that the weight of the condenser did not exceed the weight of the water saved. At 80 °C, the waste heat from the fuel cell would be of too low a grade to be useful for most purposes; however, if the fuel-cell power system were part of a motor vehicle, the waste heat could be used to heat the passenger compartment in winter.

In the advanced hydrogen generator, the reactor vessel (or one of two or more

vessels, depending on the design) would be initially charged with magnesium hydride. The advanced hydrogen generator would exploit two reactions: the aforementioned exothermic reaction at a temperature ≥ 330 °C plus the endothermic reaction $MgH_2 \rightarrow Mg + H_2$ at a temperature ≥ 300 °C. Once the initial heating was complete and both reactions under way, the Mg produced in the endothermic reaction would be consumed in the exothermic reaction, which, in turn, would generate sufficient heat to maintain the endothermic reaction. The main advantages of the advanced hydrogen generator over the basic one would be that (1) it would produce twice the amount of hydrogen for a given amount of magnesium, but (2) the cost of operation is likely to be less than that of the basic hydrogen generator because it is likely that MgH_2 could be produced at less than twice the cost of the corresponding amount of Mg.

The main waste product of both the basic and advanced systems would be

MgO, which has extremely low toxicity. MgO could be safely and easily recycled in a magnesium-refining plant for less than the cost of Mg because MgO is an intermediate product of the refining process.

This work was done by Andrew Kindler and Sri R. Narayan of Caltech for NASA's Jet Propulsion Laboratory. Further information is contained in a TSP (see page 1).

In accordance with Public Law 96-517, the contractor has elected to retain title to this invention. Inquiries concerning rights for its commercial use should be addressed to:

*Innovative Technology Assets Management
JPL*

Mail Stop 202-233

4800 Oak Grove Drive

Pasadena, CA 91109-8099

(818) 354-2240

E-mail: iaoffice@jpl.nasa.gov

Refer to NPO-43554, volume and number of this NASA Tech Briefs issue, and the page number.

Alternative OTEC Scheme for a Submarine Robot

Expansion/contraction of a wax upon freezing/thawing would be exploited.

NASA's Jet Propulsion Laboratory, Pasadena, California

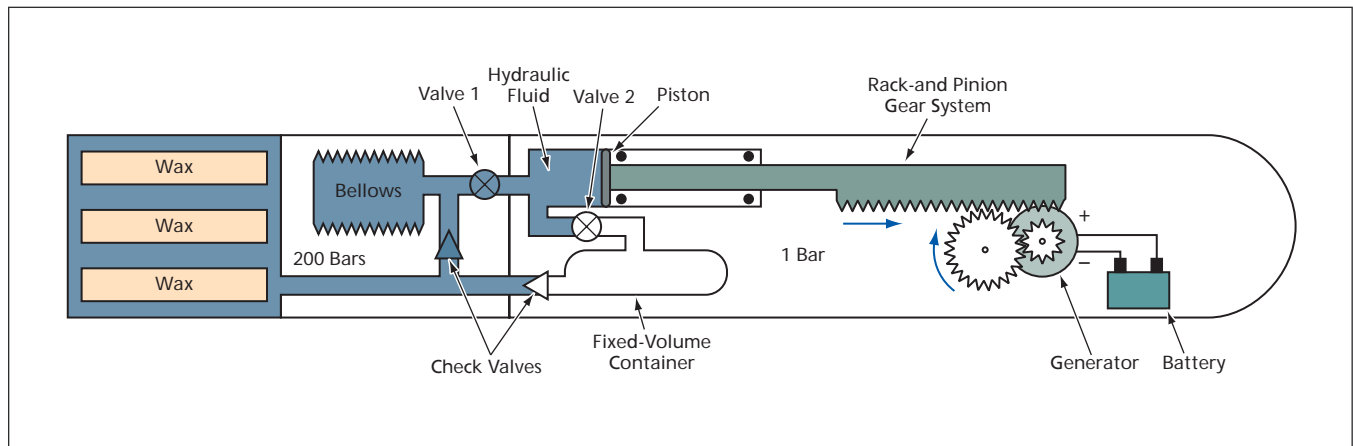
A proposed system for exploiting the ocean thermal gradient to generate power would be based on the thawing-expansion/freezing-contraction behavior of a wax or perhaps another suitable phase-change material. The power generated by this system would be used to recharge the batteries in a battery-powered unmanned underwater vehicle [UUV (essentially, a small exploratory submarine robot)] of a type that has

been deployed in large numbers in research pertaining to global warming. A UUV of this type travels between the ocean surface and various depths, measuring temperature and salinity.

This proposed system would be an alternative to another proposed ocean thermal energy conversion (OTEC) system that would serve the same purpose but would utilize a thermodynamic cycle in which CO_2 would be the working

fluid. That system is described in "Utilizing Ocean Thermal Energy in a Submarine Robot" (NPO-43304), immediately following this brief. The main advantage of this proposed system over the one using CO_2 is that it could derive a useful amount of energy from a significantly smaller temperature difference.

At one phase of its operational cycle, the system now proposed would utilize the surface ocean temperature (which



The Wax Would Expand and Contract upon melting near the ocean surface and freezing at depth, respectively. The expansion and contraction would cause the hydraulic fluid to flow cyclically against the piston to periodically drive the generator to charge the battery.

lies between 15 and 20 °C over most of the Earth) to melt a wax (e.g., pentadecane) that has a melting/freezing temperature of about 10 °C. At the opposite phase of its operational cycle, the system would utilize the lower ocean temperature at depth (e.g., between 4 and 7 °C at a depth of 300 m) to freeze the wax. The melting or freezing causes the wax to expand or contract, respectively, by about 8 volume percent.

The operational cycle is best described by reference to the figure. The wax would be contained in tubes that would be capable of expanding and contracting with the wax. The wax-containing tubes would be immersed in a hydraulic fluid.

Near the ocean surface, the expansion of the wax upon heating to >10 °C would push hydraulic fluid into a bellows in a chamber pressurized to about 200 bars (about 20 MPa). Valve 1 would then be opened, allowing the pressurized hydraulic fluid to push against a piston that, in turn, would push a rack-and-pinion gear system to spin a generator to charge a battery. Next, valve 2 would be opened, allowing the hydraulic fluid to drain into a fixed-volume container. Later, upon cooling to <10 °C at depth, the contraction of the wax upon freezing would cause hydraulic fluid to flow from the fixed-volume chamber into the chamber containing the wax tubes, thus completing the cycle.

This work was done by Jack Jones and Yi Chao of Caltech for NASA's Jet Propulsion Laboratory. Further information is contained in a TSP (see page 1).

In accordance with Public Law 96-517, the contractor has elected to retain title to this invention. Inquiries concerning rights for its commercial use should be addressed to:

*Innovative Technology Assets Management
JPL*

*Mail Stop 202-233
4800 Oak Grove Drive
Pasadena, CA 91109-8099
(818) 354-2240*

E-mail: iaoffice@jpl.nasa.gov

Refer to NPO-43500, volume and number of this NASA Tech Briefs issue, and the page number.



Sensitive, Rapid Detection of Bacterial Spores

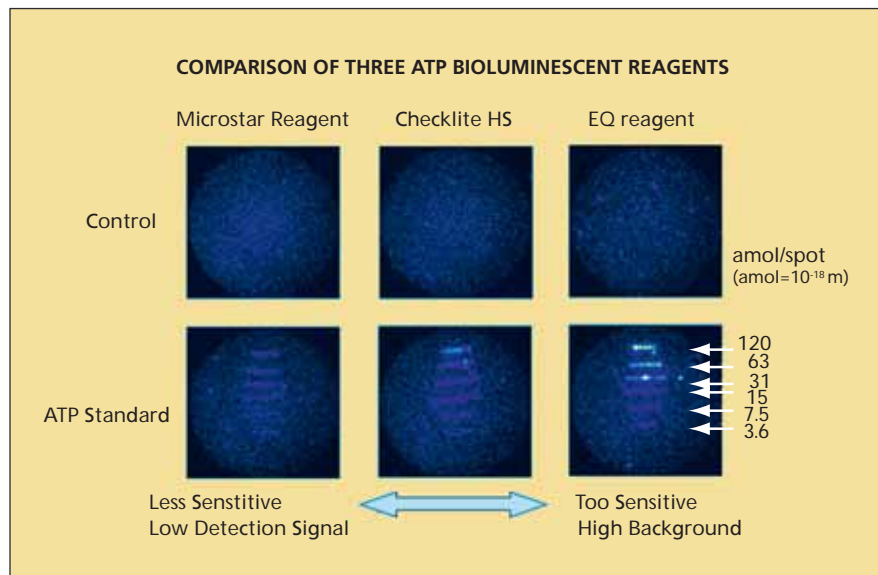
This capability is beneficial for medicine, public health, and biowarfare defense.

NASA's Jet Propulsion Laboratory, Pasadena, California

A method of sensitive detection of bacterial spores within delays of no more than a few hours has been developed to provide an alternative to a prior three-day NASA standard culture-based assay. A capability for relatively rapid detection of bacterial spores would be beneficial for many endeavors, a few examples being agriculture, medicine, public health, defense against biowarfare, water supply, sanitation, hygiene, and the food-packaging and medical-equipment industries.

The method involves the use of a commercial rapid microbial detection system (RMDS) that utilizes a combination of membrane filtration, adenosine triphosphate (ATP) bioluminescence chemistry, and analysis of luminescence images detected by a charge-coupled-device camera. This RMDS has been demonstrated to be highly sensitive in enumerating microbes (it can detect as little as one colony-forming unit per sample) and has been found to yield data in excellent correlation with those of culture-based methods. What makes the present method necessary is that the specific RMDS and the original protocols for its use are not designed for discriminating between bacterial spores and other microbes.

In this method, a heat-shock procedure is added prior to an incubation procedure that is specified in the original RMDS protocols. In this heat-shock procedure (which was also described in a prior *NASA Tech Briefs* article on enumerating spore-forming bacteria), a sample is exposed to a temperature of 80 °C for 15 minutes. Spores can survive the heat shock, but non-



These Luminescence Images were obtained in tests of three bioluminescence reagents with successively diluted samples of an ATP solution. The tests led to the selection of one of the reagents (Checklite HS) as offering the best compromise between requirements for high sensitivity and low background.

spore-forming bacteria and spore-forming bacteria that are not in spore form cannot survive. Therefore, any colonies that grow during incubation after the heat shock are deemed to have originated as spores.

This method also provides for reduction of the incubation time from the typical range (18 to 24 hours) required by the original RMDS protocols. This reduction was effected by evaluation of three commercial bioluminescence reagents (see figure), leading to the selection of one of them that makes it possible to effect detection after an incuba-

tion time of only ≈5 hours. The sensitivity and rapidity afforded by this method were demonstrated in tests in which seven species of *Bacillus* that had been repeatedly isolated from clean rooms were detected after incubation times of about 5 hours.

This work was done by Roger G. Kern, Kasthuri Venkateswaran, and Fei Chen of Caltech; Molly Pickett of Millipore Corp.; and Asahi Matsuyama of Kikkoman Corp. for NASA's Jet Propulsion Laboratory. For more information, contact iaoffice@jpl.nasa.gov. NPO-40976

Adenosine Monophosphate-Based Detection of Bacterial Spores

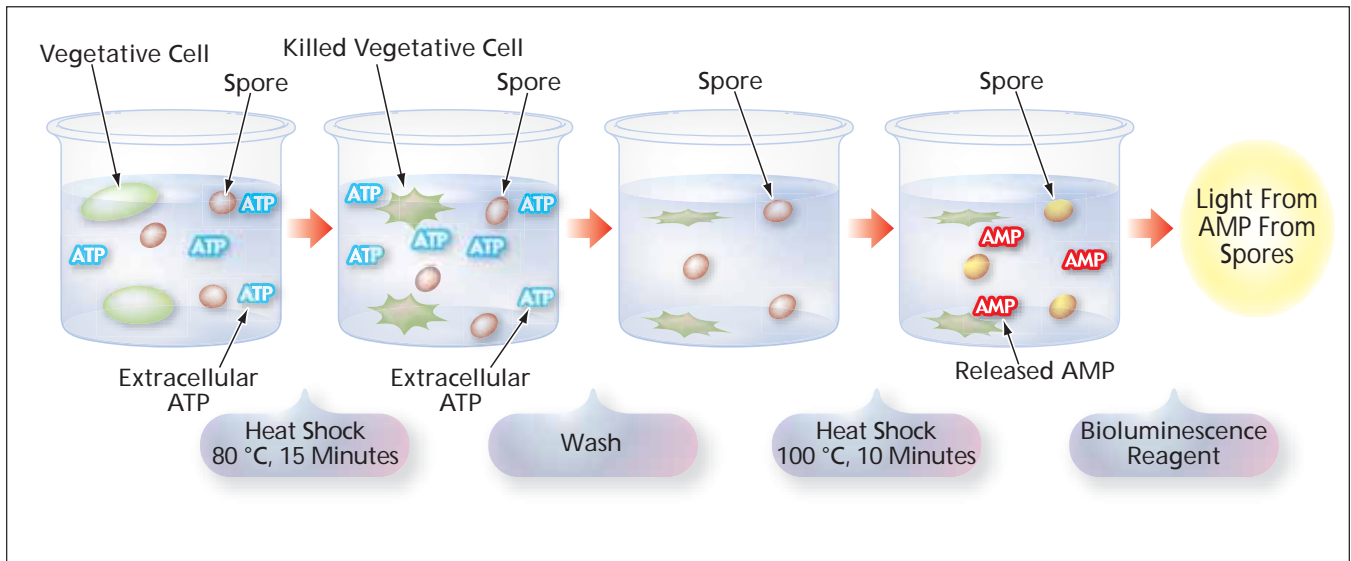
AMP is released by means of heat shock, then detected via bioluminescence.

NASA's Jet Propulsion Laboratory, Pasadena, California

A method of rapid detection of bacterial spores is based on the discovery that a heat shock consisting of exposure to a temperature of 100 °C for 10 minutes causes the complete release of adeno-

sine monophosphate (AMP) from the spores. This method could be an alternative to the method described in the immediately preceding article. Unlike that method and related prior methods,

the present method does not involve germination and cultivation; this feature is an important advantage because in cases in which the spores are those of pathogens, delays involved in germina-



This Flow Chart summarizes the laboratory procedure for rapid detection of bacterial spores.

tion and cultivation could increase risks of infection. Also, in comparison with other prior methods that do not involve germination, the present method affords greater sensitivity.

At present, the method is embodied in a laboratory procedure, though it would be desirable to implement the method by means of a miniaturized apparatus in order to make it convenient and economical enough to encourage widespread use. The main steps of the laboratory procedure (see figure) are the following:

1. A sample suspected of containing spores is suspended in an aqueous solution.
2. In the first of two heat shocks, the suspension is heated to a temperature of 80 °C for 15 minutes to kill non-spore-forming bacteria and vegetative cells.
3. The suspension is subjected to a standard low-acceleration centrifugation wash.

4. The cells from the centrifuged suspension are resuspended in a solution that contains adenosine phosphate deaminase, which eliminates extracellular adenosine triphosphate (ATP) and AMP.
5. The new suspension is subjected to the aforementioned standard low-acceleration centrifugation wash.
6. The cells from the centrifuged suspension are resuspended in distilled water.
7. In the second heat shock, the suspension is heated to 100 °C for 10 minutes, causing the release of AMP from any spores that may be present.
8. A fraction of the heat-shocked suspension is treated using a commercially available bioluminescence agent with pyruvate, orthophosphate dikinase, causing luminescence in proportion to the concentration(s) of ATP that are converted from AMP by oxidative phosphorylation. The

luminescence is measured by use of a standard laboratory luminometer.

9. To further ensure that the bioluminescence is of spore (AMP) origin and to discriminate against any residual ATP in the suspension, a remaining untreated fraction of the suspension from step 6 is similarly tested for luminescence that responds to ATP but not AMP.

In experiments on eight strains of *Bacillus*, this method was found to enable detection of spores in suspension down to sub-femtomolar levels of AMP. These levels correspond to sensitivity of the order of 100 or fewer spores per sample.

This work was done by Roger G. Kern, Fei Chen, and Kasthuri Venkateswaran of Caltech and Nori Hattori and Shigeya Suzuki of Kikkoman Corp. for NASA's Jet Propulsion Laboratory. For more information, contact iaoffice@jpl.nasa.gov. NPO-40938



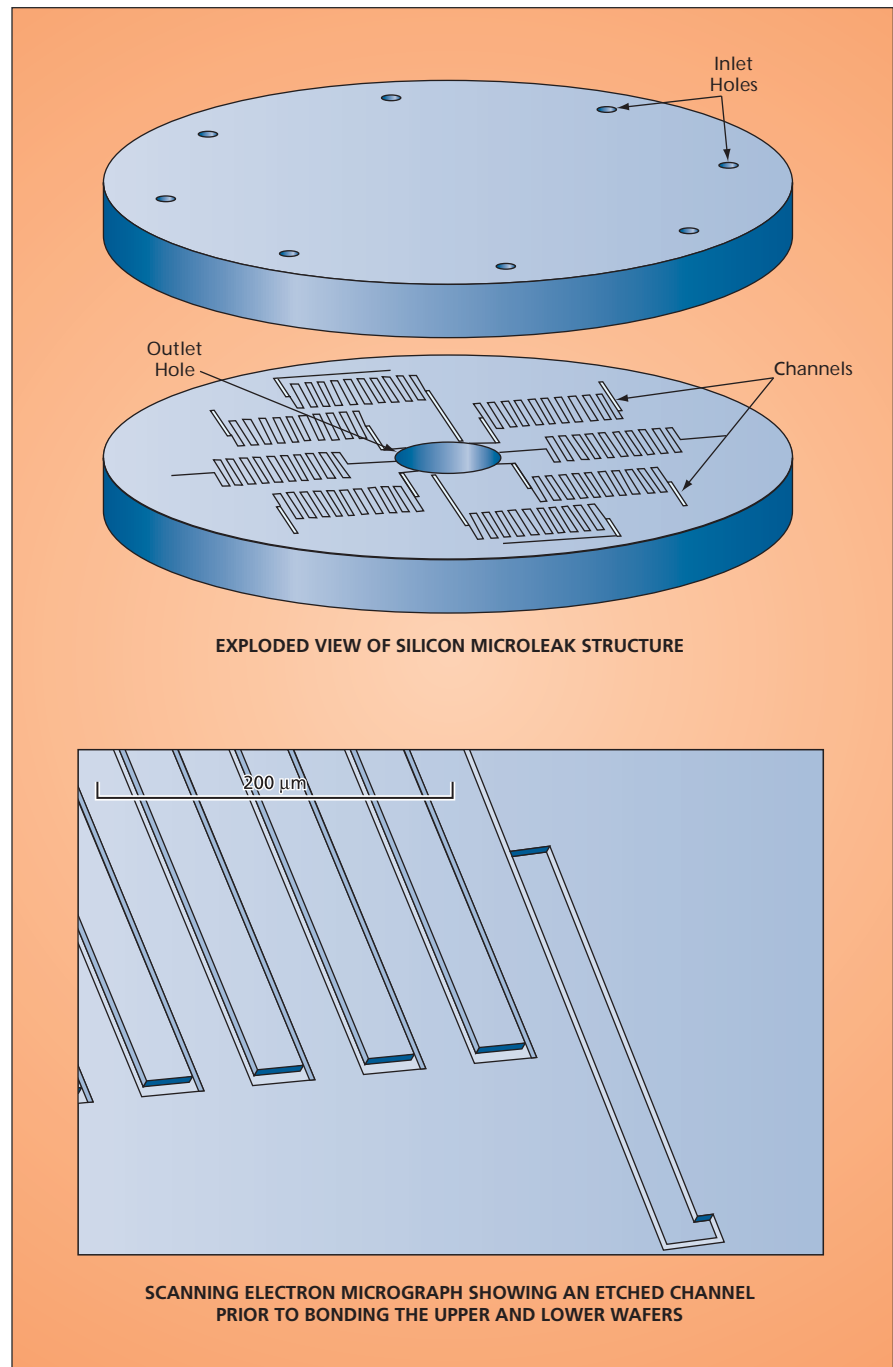
● Silicon Microleaks for Inlets of Mass Spectrometers

These devices could contribute to feasibility of small, portable mass spectrometers.

Goddard Space Flight Center, Greenbelt, Maryland

Microleaks for inlets of mass spectrometers used to analyze atmospheric gases can be fabricated in silicon wafers by means of photolithography, etching, and other techniques that are commonly used in the manufacture of integrated circuits and microelectromechanical systems. The microleaks serve to limit the flows of the gases into the mass-spectrometer vacuums to specified very small flow rates consistent with the capacities of the spectrometer vacuum pumps. There is a need to be able to precisely tailor the dimensions of each microleak so as to tailor its conductance to a precise low value. (As used here, “conductance” signifies the ratio between the rate of flow in the leak and the pressure drop from the upstream to the downstream end of the leak.) To date, microleaks have been made, variously, of crimped metal tubes, pulled glass tubes, or frits. Crimped-metal and pulled-glass-tube microleaks cannot readily be fabricated repeatably to precise dimensions and are susceptible to clogging with droplets or particles. Frits tend to be differentially chemically reactive with various gas constituents and, hence, to distort the gas mixtures to be analyzed. The present approach involving microfabrication in silicon largely overcomes the disadvantages of the prior approaches.

A silicon microleak comprises a silicon disk or plug containing channels that typically have cross-sectional dimensions of the order of microns and lengths from hundreds of microns to about a millimeter (see figure). Lithography enables precise tailoring of the lengths and cross-sectional dimensions of the channels, thereby enabling precise tailoring of conductances. A plug or disk can be fabricated to contain multiple channels that sustain parallel flows to reduce the adverse effect of clogging of a single channel with particles or droplets. The silicon and other materials incorporated during fabrication do not react chemically with most atmospheric gases to be sampled and,



EXPLODED VIEW OF SILICON MICROLEAK STRUCTURE

SCANNING ELECTRON MICROGRAPH SHOWING AN ETCHED CHANNEL PRIOR TO BONDING THE UPPER AND LOWER WAFERS

Serpentine Channels are photolithographically defined, then etched onto the surface of the lower silicon wafer. Next, the etched lower silicon wafer is fusion-bonded to the upper silicon wafer. Finally, inlet and outlet holes providing access to the ends of the channels are etched through the upper and lower wafers, respectively.

hence, do not distort samples in most cases. The techniques used in fabrication are amenable to fabrication in batches, thereby enabling production at relatively low cost.

Silicon microleaks have potential for additional device functionality. For example, resistance heaters could be integrated into silicon microleak structures to enable heating of inlets to vaporize droplets to prevent clogging. Thermistors could also be integrated into silicon microleak structures for monitoring their temperatures. Yet another device concept is that of a one-shot-closing valve: an integrated resistance heater

would be used to momentarily melt a microscopic piece of a suitable metal positioned near a channel to cause the metal to flow into, and thus plug, the channel. If all of the multiple channels in a silicon microleak structure were equipped with one-shot-closing valves, then the valves could be actuated, one at a time, to effect stepped reductions in the overall conductance of the microleak.

Silicon microleaks could contribute to the feasibility of proposed small, field-deployable mass spectrometers for homeland-security and point-of-care medical diagnostic applications. Silicon microleaks might also be useful as very-low-conduc-

tance calibrated leaks that could enable different approaches to environmental gas sampling. Orifices that support leak rates ranging from 0.1 to 5 standard cubic centimeters per minute are currently available for use in environmental sampling. Silicon microleaks, which can be made to support flow rates many orders of magnitude lower, would enable gas sampling with much smaller volumes.

This work was done by Dan Harpold, Hasso Niemann, and Brian G Jamieson of Goddard Space Flight Center and Bernard A Lynch of MEI Technologies, Inc. Further information is contained in a TSP (see page 1). GSC-15341-1

CGH Figure Testing of Aspherical Mirrors in Cold Vacuums

Room-temperature and cryogenic tests yield complementary data on surface-figure errors.

Goddard Space Flight Center, Greenbelt, Maryland

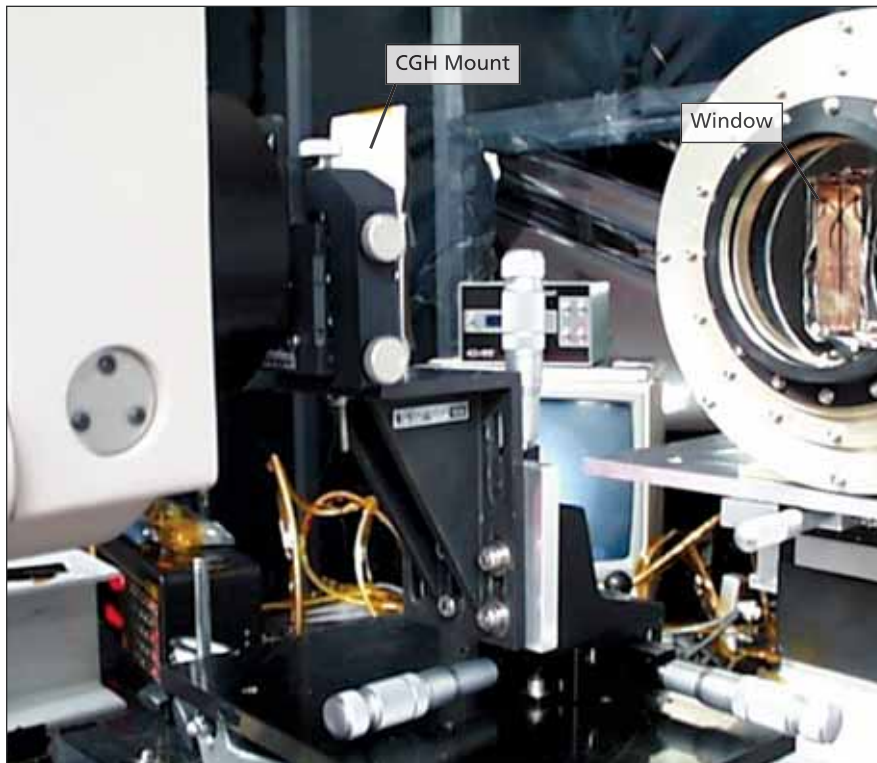
An established method of room-temperature interferometric null testing of mirrors having simple shapes (e.g., flat, spherical, or spheroidal) has been augmented to enable measurement of errors in the surface figures of off-axis, non-axisymmetric, aspherical mirrors when the mirrors are located inside cryogenic vacuum chambers. The estab-

lished method involves the use of a computer-generated hologram (CGH), functionally equivalent to a traditional null lens, to modify the laser beam of an imaging interferometer to obtain a reference wavefront that matches the ideal surface figure of a mirror under test. The CGH is inserted at the appropriate position and orientation in the

optical path of the imaging interferometer, which, in turn, is appropriately positioned and oriented with respect to the mirror under test. Deviations of the surface figure of the mirror from the ideal surface figure manifest themselves as interference fringes. Interferograms are recorded and analyzed to deduce figure errors.

The need for the present augmented method arises because testing an off-axis, non-axisymmetric, aspherical mirror in a cryogenic environment entails the following complications that are not present in room-temperature testing of simpler mirrors:

- There are commercial off-the-shelf CGHs for the simpler mirror shapes, but not for the more-complex aspherical, off-axis shapes.
- The wall of a typical cryogenic vacuum chamber blocks access to optomechanical alignment fiducial objects that are incorporated into or attached to the mirror.
- Thermal contraction from room temperature to the cryogenic test temperature changes gives rise to a change in the mirror surface, relative to the reference wavefront, that can be confused with a change in surface-figure error.
- The interferometer is located outside the cryogenic vacuum chamber and gains optical access to the mirror in the chamber via a window in the wall of the chamber (see figure). It is necessary to take account of the optical effects of the window, including any changes in these effects caused by imposition of



A CGH is positioned to modify a test laser beam that travels, via a window, to and from a mirror under test inside a cryogenic vacuum chamber. The optical effects of the window, including the effects of any temperature gradient through the window, must be taken into account in analyzing test data.

the ambient-to-cryogenic temperature gradient across the window.

The augmented method includes elements of laboratory implementation and data reduction that go beyond those of the established room-temperature-only method. The most straightforward aspect of the method is the use of an off-the-shelf interferometer and, to match the complex shape of the mirror under test, a custom CGH. Other aspects of the method, too complex to describe in detail, can be sum-

marized as follows: The method calls for a complex combination of room-temperature and cryogenic test procedures and associated data-reduction procedures formulated to minimize systematic test errors and reveal subtle thermomechanical and optical effects, and thereby to characterize surface-figure errors at ambient and cryogenic temperatures. One notable feature of the method is the use of interferometric techniques to quickly align the mirror under test when it is in the cryogenic

chamber. Once the mirror has been aligned and thermal equilibrium has been established, measurements are performed on both mirror and window surfaces to obtain the data needed to computationally eliminate the optical effects of the window.

This work was done by Victor John Chambers, Raymond G. Ohl, and Ronald G. Mink of Goddard Space Flight Center and Steven Arnold of Diffraction International Ltd. Further information is contained in a TSP (see page 1). GSC-14789-1

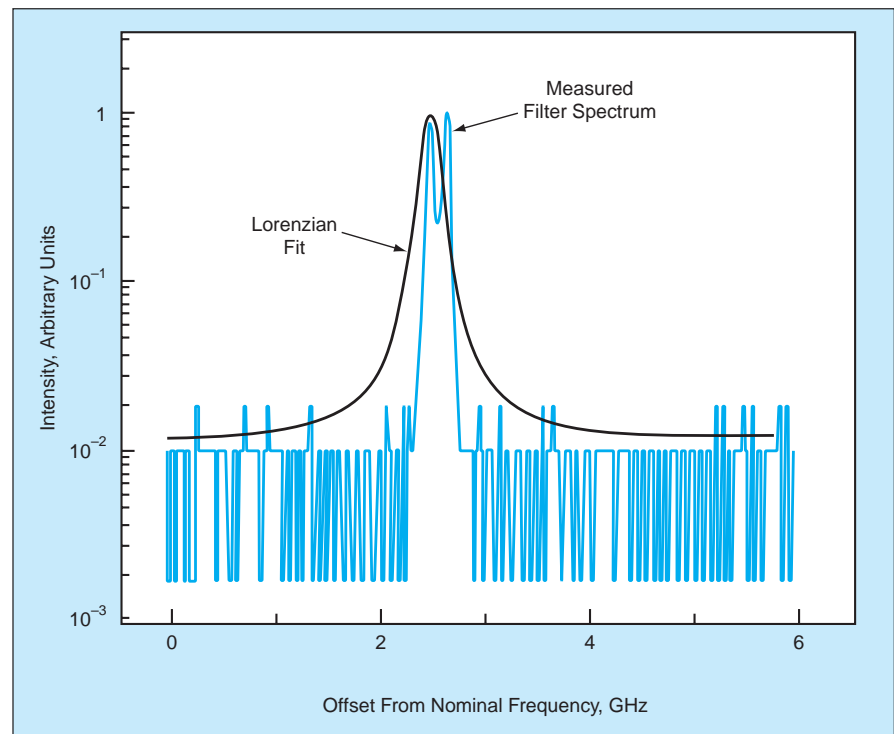
Series-Coupled Pairs of Silica Microresonators

Pass bands are narrower and flatter than those of single microresonators.

NASA's Jet Propulsion Laboratory, Pasadena, California

Series-coupled pairs of whispering-gallery-mode optical microresonators have been demonstrated as prototypes of stable, narrow-band-pass photonic filters. Characteristics that are generally considered desirable in a photonic or other narrow-band-pass filter include response as nearly flat as possible across the pass band, sharp roll-off, and high rejection of signals outside the pass band. A single microresonator exhibits a Lorentzian filter function: its peak response cannot be made flatter and its roll-off cannot be made sharper. However, as a matter of basic principle applicable to resonators in general, it is possible to (1) use multiple resonators, operating in series or parallel, to obtain a roll-off sharper, and out-of-band rejection greater, relative to those of a Lorentzian filter function and (2) to make the peak response (the response within the pass band) flatter by tuning the resonators to slightly different resonance frequencies that span the pass band.

The first of the two microresonators in each series-coupled pair was a microtorus made of germania-doped silica (containing about 19 mole percent germania), which is a material used for the cores of some optical fibers. The reasons for choosing this material is that exposing it to ultraviolet light causes it to undergo a chemical change that changes its index of refraction and thereby changes the resonance frequency. Hence, this material affords the means to effect the desired slight relative detuning of the two resonators. The second microresonator in each pair was a microsphere of pure silica. The advantage of making one of the



This Second-Order Filter Spectral Response was determined in measurements on a band-pass filter comprising a germania-doped silica microtorus series-coupled to a silica microsphere. A Lorentzian fit to the corresponding spectral response of a single microresonator is also shown for comparison.

resonators a torus instead of a sphere is that its spectrum of whispering-gallery-mode resonances is sparser, as needed to obtain a frequency separation of at least 100 GHz between resonances of the filter as a whole.

The two microresonators in each pair were mounted in proximity to each other so that the two were optically coupled. Half of the amplified light from a laser diode at a nominal wavelength of 1.55 μm was coupled into the first microresonator by means of an angle-pol-

ished optical fiber. The other half of the amplified laser light was passed through a Fabry-Perot cavity having a free spectral range of 20 GHz; this cavity served as both a reference to correct for laser frequency drift and a scale for measuring the difference between resonance frequencies. By use of a second angle-polished optical fiber, light was coupled out of the second microresonator to a photodiode.

An argon-ion laser operating at a wavelength of 351 nm (the wavelength

most efficient for producing the desired photochemical reaction) was focused into the germania-doped microresonator. The current applied to the photodiode was modulated with a sawtooth waveform in order to sweep the laser wavelength repeatedly through a frequency range that included the pass band and surrounding frequencies. Using knowledge of the laser frequency vs. time, along with the measurements of photocurrent vs. time, it was possible to determine the magnitude of the filter

spectrum. From time to time, the argon laser was turned on to tune the germania-doped microresonator, and then the spectrum determined. Care was taken to discriminate against the transient contribution of laser-induced thermal expansion to the change in the spectrum. The process was repeated until the desired separation between the two resonance frequencies was obtained (for example, see figure).

This work was done by Anatoliy Savchenkov, Vladimir Iltchenko, Lute Maleki,

and Tim Handley of Caltech for NASA's Jet Propulsion Laboratory.

*Innovative Technology Assets Management
JPL*

*Mail Stop 202-233
4800 Oak Grove Drive
Pasadena, CA 91109-8099
(818) 354-2240*

E-mail: iaoffice@jpl.nasa.gov

Refer to NPO-30828, volume and number of this NASA Tech Briefs issue, and the page number.

Precise Stabilization of the Optical Frequency of WGMRs

This technique results in whispering gallery mode resonators with absolute frequency stability.

NASA's Jet Propulsion Laboratory, Pasadena, California

Crystalline whispering gallery mode resonators (CWGMRs) made of crystals with axial symmetry have ordinary and extraordinary families of optical modes. These modes have substantially different thermo-refractive constants. This results in a very sharp dependence of differential detuning of optical frequency on effective temperature. This frequency difference compared with clock gives an error signal for precise compensation of the random fluctuations of optical frequency. Certain crystals, like MgF_2 , have "turnover" points where the thermo-refractive effect is completely nullified.

An advantage for applications using WGMRs for frequency stabilization is in the possibility of manufacturing resonators out of practically any optically transparent crystal. It is known that there are crystals with negative and zero thermal expansion at some specific temperatures. Doping changes properties of the crystals and it is possible to create an optically transparent crystal with zero thermal expansion at room temperature. With this innovation's stabilization technique, the resultant WGMR will have absolute frequency stability

The expansion of the resonator's body can be completely compensated for by nonlinear elements. This results in compensation of linear thermal expansion (see figure). In three-mode, the MgF_2 resonator, if tuned at the turnover

thermal point, can compensate for all types of random thermal-related frequency drift. Simplified dual-mode method is also available. This creates miniature optical resonators with good short- and long-term stability for passive secondary frequency ethalon and an active resonator for active secondary frequency standard (a narrowband laser with long-term stability).

Optical losses due to media imperfection were addressed through a multi-step, asymptotic processing of the res-

onator. This technique has been initially developed to reduce microwave absorption in dielectric resonators. One part of this process consists of mechanical polishing performed after high-temperature annealing by placing the fluorite WGMR in a 3-foot-long (0.91-m-long), air-filled, transparent tube of annealed fused silica and then into a 20-cm-long horizontal tube furnace with a heated furnace core. The annealing process improves the transparency of the material because an increased temperature results in the en-

hancement of the mobility of defects induced by the fabrication process, and also reduces any residual stress birefringence. The increased mobility leads to the recombination of defects and their migration to the surface. The straightforward annealing of a WGMR leads to $Q > 10^{11}$ at $1.55 \mu m$.

This work was done by Anatoliy Savchenkov, Andrey Matsko, Nan Yu, Lute Maleki, and Vladimir Iltchenko of Caltech for NASA's Jet Propulsion Laboratory.

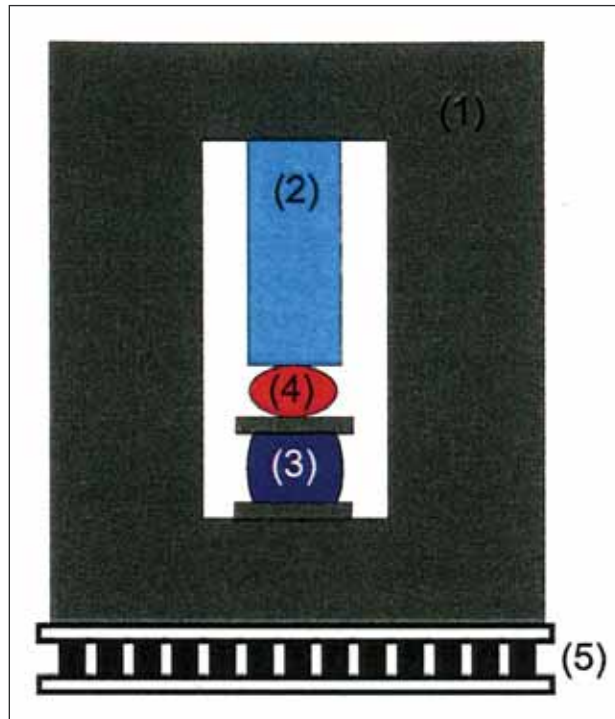
In accordance with Public Law 96-517, the contractor has elected to retain title to this invention. Inquiries concerning rights for its commercial use should be addressed to:

Innovative Technology Assets Management

*JPL
Mail Stop 202-233
4800 Oak Grove Drive
Pasadena, CA 91109-8099*

E-mail: iaoffice@jpl.nasa.gov

Refer to NPO-45180, volume and number of this NASA Tech Briefs issue, and the page number.



A Nonlinear Thermal Compensator for an optical WGM resonator consists of (1) a rigid metal frame, (2) a glass or metal wedge-shaped spacer, and (3) a WGM resonator sandwiched between rigid spacers on the top and bottom. Temperature tuning is realized with a heater (5), and the nonlinearity is introduced by a nonlinear element (4).

Formation Flying of Components of a Large Space Telescope

NASA's Jet Propulsion Laboratory, Pasadena, California

A conceptual space telescope having an aperture tens of meters wide and a focal length of hundreds of meters would be implemented as a group of six separate optical modules flying in formation: a primary-membrane-mirror module, a relay-mirror module, a focal-plane-assembly module containing a fast steering mirror and secondary and tertiary optics, a primary-mirror-figure-sensing module, a scanning-electron-beam module for controlling the shape of the primary mirror, and a sunshade module.

Formation flying would make it unnecessary to maintain the required precise alignments among the modules by means of an impractically massive rigid structure. Instead, a control system operating in conjunction with a metrology system comprising optical and radio subsystems would control the firing of small thrusters on the separate modules to maintain the formation, thereby acting as a virtual rigid structure. The control system would utilize a combination of centralized- and decentralized-control

methods according to a leader-follower approach.

The feasibility of the concept was demonstrated in computational simulations that showed that relative positions could be maintained to within a fraction of a millimeter and orientations to within several microradians.

This work was done by Edward Mettler, Marco Quadrelli, and William Breckenridge of Caltech for NASA's Jet Propulsion Laboratory. For more information, contact iaoffice@jpl.nasa.gov. NPO-45199

Laser Metrology Heterodyne Phase-Locked Loop

NASA's Jet Propulsion Laboratory, Pasadena, California

A method reduces sensitivity to noise in a signal from a laser heterodyne interferometer. The phase-locked loop (PLL) removes glitches that occur in a zero-crossing detector's output [that can happen if the signal-to-noise ratio (SNR) of the heterodyne signal is low] by the use of an internal oscillator that produces a square-wave signal at a frequency that is inherently close to the heterodyne frequency.

It also contains phase-locking circuits that lock the phase of the oscillator to

the output of the zero-crossing detector. Because the PLL output is an oscillator signal, it is glitch-free. This enables the ability to make accurate phase measurements in spite of low SNR, creates an immunity to phase error caused by shifts in the heterodyne frequency (i.e. if the target moves causing Doppler shift), and maintains a valid phase even when the signal drops out for brief periods of time, such as when the laser is blocked by a stray object.

This work was done by Frank Loya and Peter Halverson of Caltech for NASA's Jet Propulsion Laboratory. Further information is contained in a TSP (see page 1).

This invention is owned by NASA, and a patent application has been filed. Inquiries concerning nonexclusive or exclusive license for its commercial development should be addressed to the Patent Counsel, NASA Management Office-JPL. Refer to NPO-40080.

Spatial Modulation Improves Performance in CTIS

Computed spectra are more accurate when scenes have spatial structure.

NASA's Jet Propulsion Laboratory, Pasadena, California

Suitably formulated spatial modulation of a scene imaged by a computed-tomography imaging spectrometer (CTIS) has been found to be useful as a means of improving the imaging performance of the CTIS. As used here, "spatial modulation" signifies the imposition of additional, artificial structure on a scene from within the CTIS optics.

The basic principles of a CTIS were described in "Improvements in Computed-Tomography Imaging Spectrometry" (NPO-20561) *NASA Tech Briefs*, Vol. 24, No. 12 (December 2000), page 38 and "All-Reflective Computed-Tomography Imaging Spectrometers" (NPO-20836),

NASA Tech Briefs, Vol. 26, No. 11 (November 2002), page 7a. To recapitulate: A CTIS offers capabilities for imaging a scene with spatial, spectral, and temporal resolution. The spectral disperser in a CTIS is a two-dimensional diffraction grating. It is positioned between two relay lenses (or on one of two relay mirrors) in a video imaging system. If the disperser were removed, the system would produce ordinary images of the scene in its field of view. In the presence of the grating, the image on the focal plane of the system contains both spectral and spatial information because the multiple diffraction orders of the grating give rise to multiple, spectrally dispersed images of the scene.

By use of algorithms adapted from computed tomography, the image on the focal plane can be processed into an "image cube" — a three-dimensional collection of data on the image intensity as a function of the two spatial dimensions (x and y) in the scene and of wavelength (λ). Thus, both spectrally and spatially resolved information on the scene at a given instant of time can be obtained, without scanning, from a single snapshot; this is what makes the CTIS such a potentially powerful tool for spatially, spectrally, and temporally resolved imaging.

A CTIS performs poorly in imaging some types of scenes — in particular, scenes that contain little spatial or spectral

variation. The computed spectra of such scenes tend to approximate correct values to within acceptably small errors near the edges of the field of view but to be poor approximations away from the edges. The additional structure imposed on a scene according to the present method enables the CTIS algorithms to reconstruct acceptable approximations of the spectral data throughout the scene.

The structure can be imposed in any of a number of alternative ways. In preliminary experiments, the structure was imposed by means of a digital multi-mirror device at the field stop in an all-

reflective-optics CTIS. Any of the mirrors could be turned on or off to make a desired pattern. The optimum pattern has not yet been determined; a checkerboard pattern was used in the experiments. (In one alternative, in the case of refractive optics, the structure could be imposed by use of a suitably patterned opaque mask at the field stop.) A full image could be acquired by shifting the pattern by use of software or by moving the mirror device or mask.

This work was done by Gregory H. Bearman, Daniel W. Wilson, and William R.

Johnson of Caltech for NASA's Jet Propulsion Laboratory.

In accordance with Public Law 96-517, the contractor has elected to retain title to this invention. Inquiries concerning rights for its commercial use should be addressed to:

*Innovative Technology Assets Management
JPL*

*Mail Stop 202-233
4800 Oak Grove Drive
Pasadena, CA 91109-8099*

E-mail: iaoffice@jpl.nasa.gov

Refer to NPO-41557, volume and number of this NASA Tech Briefs issue, and the page number.



High-Performance Algorithm for Solving the Diagnosis Problem

Computation time is reduced substantially.

NASA's Jet Propulsion Laboratory, Pasadena, California

An improved method of model-based diagnosis of a complex engineering system is embodied in an algorithm that involves considerably less computation than do prior such algorithms. This method and algorithm are based largely on developments reported in several NASA Tech Briefs articles: "The Complexity of the Diagnosis Problem" (NPO-30315), Vol. 26, No. 4 (April 2002), page 20; "Fast Algorithms for Model-Based Diagnosis" (NPO-30582), Vol. 29, No. 3 (March 2005), page 69; "Two Methods of Efficient Solution of the Hitting-Set Problem" (NPO-30584), Vol. 29, No. 3 (March 2005), page 73; and "Efficient Model-Based Diagnosis Engine" (NPO-40544), on the following page.

Some background information from the cited articles is prerequisite to a meaningful summary of the innovative aspects of the present method and algorithm. In model-based diagnosis, the function of each component and the relationships among all the components of the engineering system to be diagnosed are represented as a logical system denoted the system description (SD). Hence, the expected normal behavior of the engineering system is the set of logical consequences of the SD. Faulty components lead to inconsistencies between the observed behaviors of the system and the SD. Diagnosis — the task of finding faulty components — is reduced to finding those components, the abnormalities of which could explain all the inconsistencies. The solution of the diagnosis problem should be a minimal diagnosis, which is a minimal set of faulty components.

The calculation of a minimal diagnosis is inherently a hard problem, the solution of which requires amounts of computation time and memory that increase exponentially with the number of components of the engineering system.

Among the developments to reduce the computational burden, as reported in the cited articles, is the mapping of the diagnosis problem onto the integer-programming (IP) problem. This mapping makes it possible to utilize a variety of algorithms developed previously for IP to solve the diagnosis problem. In the IP approach, the diagnosis problem can be formulated as a linear integer optimization

problem, the traditional version of the branch-and-bound algorithm includes the following:

- Using non-integer and integer solutions of the corresponding linear-programming (LP) relaxation problem (see figure), in which the variables of the IP problem are no longer constrained to be integers, to define lower and upper bounds, respectively;
- Successively dividing (branching) the IP problem into subproblems on the basis of the bounds; and
- Eliminating any subproblem, the LP lower bound of which exceeds the upper bound of another subproblem.

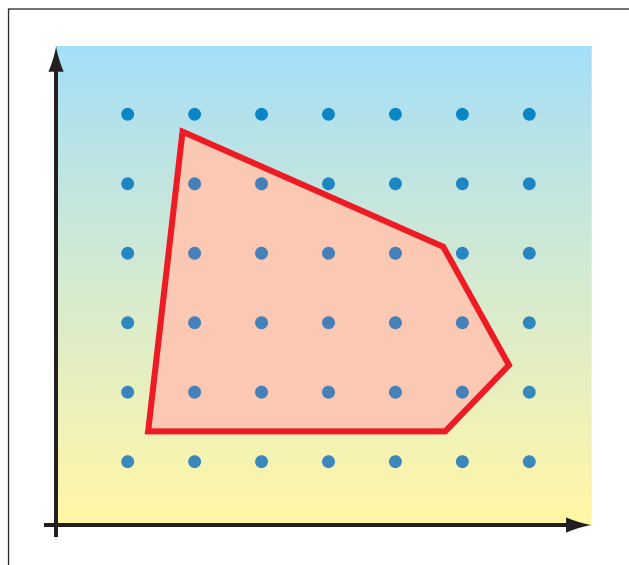
The branching, bounding, and elimination are repeated until all subproblems are eliminated or an integer solution is found.

The present algorithm is an alternative version of the branch-and-bound algorithm. In this algorithm, the amount of computation required for execution is reduced, relative to that of the traditional version, by exploiting the structure of the problem. The amount of computation is further reduced by using the solution window to effect a massive pruning of branches. Yet another reduction is effected by dynamically updating and narrowing the window to enable further pruning. In simulation tests on systems of 40 components, the present algorithm was found to solve the diagnosis problem at an average speed about 300 times faster than that of the traditional branch-and-bound algorithm.

The present algorithm is an alternative version of the branch-and-bound algorithm. In this algorithm, the amount of computation required for execution is reduced, relative to that of the traditional version, by exploiting the structure of the problem. The amount of computation is further reduced by using the solution window to effect a massive pruning of branches. Yet another reduction is effected by dynamically updating and narrowing the window to enable further pruning. In simulation tests on systems of 40 components, the present algorithm was found to solve the diagnosis problem at an average speed about 300 times faster than that of the traditional branch-and-bound algorithm.

This work was done by Amir Fijany and Farrokh Vatan of Caltech for NASA's Jet Propulsion Laboratory. Further information is contained in a TSP (see page 1).

The software used in this innovation is available for commercial licensing. Please contact Karina Edmonds of the California Institute of Technology at (626) 395-2322. Refer to NPO-41456.



The Sets of Solutions of the LP relaxation and IP problems are represented by (1) the polygon and (2) the grid points inside the polygon, respectively.

tion problem, which can be solved by use of well-developed integer-programming algorithms. This concludes the background information.

The point of departure for the development of the present improved method and algorithm is the discovery that the mapping of the diagnosis problem onto the IP problem makes it possible to calculate lower and upper bounds on the number of faulty components before solving the diagnosis problem. A solution window for the problem is introduced, based on these bounds.

One of the algorithms heretofore commonly used to solve the IP problem is known in the art as the branch-and-bound algorithm. In terms that are necessarily oversimplified for the sake of

Truncation Depth Rule-of-Thumb for Convolutional Codes

The new rule is more accurate and tight at high signal-to-noise ratios.

NASA's Jet Propulsion Laboratory, Pasadena, California

In this innovation, it is shown that a commonly used rule of thumb (that the truncation depth of a convolutional code should be five times the memory length, m , of the code) is accurate only for rate $1/2$ codes. In fact, the truncation depth should be $2.5m/(1-r)$, where r is the code rate. The accuracy of this new rule is demonstrated by tabulating the distance properties of a large set of known codes. This new rule was derived by bounding the losses due to truncation as a function of the code rate.

The bound derives from a result on random trellis codes in G.D. Forney, Jr.'s "Convolutional codes II: Maximum likelihood decoding," *Information and Control*, vol. 25:222-266 (1974). An (M, v) trellis is a trellis corresponding to a shift register of length v where each register contains a M -vector and the input is an M -ary sequence (the corresponding trellis contains M^v states). An (M, v, n) trellis code augments an (M, v) trellis by assigning n channel symbols to each edge. The rate of the

code is $r = \log_2(M)/n$ bits/symbol. A random trellis code is an (M, v, n) trellis in which each channel symbol on each edge is chosen randomly and independently according to some distribution p . When $M = q^k$ the (M, v, n) trellis corresponds to a rate $\log_2(q)k/n$ nonsystematic convolutional code over GF(q) with k equal constraint lengths $v_i = v, 1 < i < k$. The memory of this code is $m = \max_{i \neq 1} v_i$. It is presumed that the code is decoded via the Viterbi algorithm with decisions on edges of the trellis made after a delay of T trellis stages. A truncation error occurs when an incorrect edge is chosen that would not have been chosen with an infinite truncation depth.

In the case of punctured codes, the truncation depth on the mother code trellis should be increased as the rate increases. Punctured code can be created by forming (q^k, v, n) code by puncturing a (q^k, v_1, n_1) mother code, where k_1 divides k and $v = v_1 k_1 / k$. This resulting code is the daughter code. The two

codes are represented with the same number of states, with k/k_1 stages of the mother code corresponding to 1 stage of the daughter code. The required truncation depth on the daughter code trellis corresponds to a truncation depth on the mother code trellis of

$$1 > v_1 / (1 - r)$$

i.e., the truncation depth on the mother code goes as the memory of the mother code scaled by one minus the rate of the punctured code.

With regard to particular codes, a good indicator of the required truncation depth is the path length at which all paths that diverge from a particular path have accumulated the minimum distance of the code. It is shown that the new rule of thumb provides an accurate prediction of this depth for codes of varying rates.

This work was done by Bruce Moision of Caltech for NASA's Jet Propulsion Laboratory. Further information is contained in a TSP (see page 1). NPO-45009

Efficient Method for Optimizing Placement of Sensors

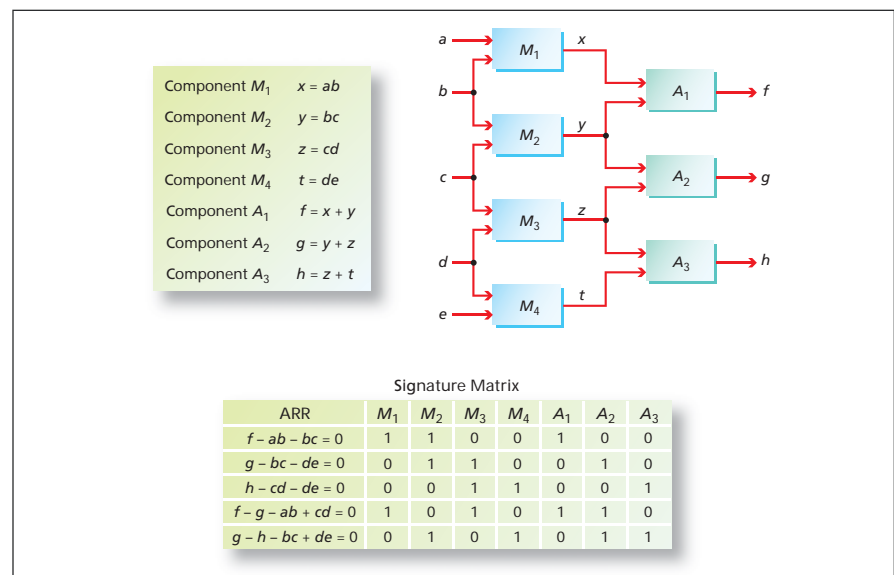
This systematic method supplants *ad hoc* placement and exhaustive-search optimization methods.

NASA's Jet Propulsion Laboratory, Pasadena, California

A computationally efficient method has been developed to enable optimization of the placement of sensors for the purpose of diagnosis of a complex engineering system (e.g., an aircraft or spacecraft). The method can be used both in (1) designing a sensor system in which the number and positions of sensors are initially not known and must be determined and (2) adding sensors to a pre-existing system to increase the diagnostic capability.

The optimal-sensor-placement problem can be summarized as involving the following concepts, issues, and subproblems:

- **Degree of Diagnosability** — This is a concept for characterizing the set of faults that can be discriminated by use of a given set of sensors.
- **Minimal Sensor Set** — The idea is one of finding a minimal set of sensors that guarantees a specific degree of diagnosability.
- **Minimal-Cost Sensors** — In a case in which different sensors are assigned with dif-



A System of Four Multiplier and Three Adder Gates serves as an example for illustrating the concept of ARR and a signature matrix. In this example, there are three sensors that measure the variables f , g , and h . Each element of the matrix is 1 or 0 if the ARR listed in the row containing that element is or is not, respectively, affected by a fault in the gate listed in the column containing that element.

ferent costs, it is desired to choose the least costly set of sensors that affords a specific degree of diagnosability.

The development of the present method for solving the optimal-sensor-placement problem began with a rigorous mathematical description of the problem, leading to a very efficient algorithm for its solution. This method incorporates elements of a method, developed by the same innovators, for solving the diagnosis problem. Aspects of this diagnostic method and developments leading up to it were reported in several previous *NASA Tech Briefs* articles, the most recent and relevant being "High-Performance Algorithm for Solving the Diagnosis Problem" (NPO-41456), on the preceding page.

It was observed that in an algorithmic sense, the sensor-placement problem is an extension of the diagnosis problem and that both problems can be mapped to a special case of the 0/1 integer-programming (IP) problem. The only difference is that in the optimal-sensor-placement problem, the objective function, in the most general case, is no longer linear. However, the constraints are still linear and defined by a 0/1 matrix.

The solution of the sensor-placement problem starts with the formulation of a structural model of the system to be diagnosed. The structural analysis of the system and the potential information to be collected by each sensor are combined into a set of equations usually called the analytical redundant relations (ARRs). One also takes account of additional sensors and the ARR of those sensors that, if used, would provide a desired degree of diagnosability. The information from all the ARRs is summarized in a signature matrix (see figure). Then the optimal-sensor-placement problem can be formulated as an IP problem involving the signature matrix.

In the present method, the IP problem is solved by a variant of the traditional branch-and-bound algorithm, which is among the algorithms heretofore commonly used to solve the IP problem. Briefly, the traditional branch-and-bound algorithm includes finding lower and upper bounds on solutions, successively dividing (branching) the IP problem into subproblems on the basis of the bounds, and eliminating any subprob-

lem, the lower bound of which exceeds the upper bound of another subproblem. The branching, bounding, and elimination are repeated until all subproblems are eliminated. The present new variant of the branch-and-bound algorithm is similar to the one used in the aforementioned method for solving the diagnosis problem and offers orders-of-magnitude speedup over prior exhaustive-search algorithms.

This work was done by Amir Fijany and Farrokh Vatan of Caltech for NASA's Jet Propulsion Laboratory. Further information is contained in a TSP (see page 1).

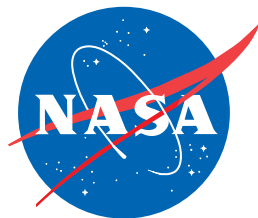
In accordance with Public Law 96-517, the contractor has elected to retain title to this invention. Inquiries concerning rights for its commercial use should be addressed to:

*Innovative Technology Assets Management
JPL*

*Mail Stop 202-233
4800 Oak Grove Drive
Pasadena, CA 91109-8099
(818) 354-2240*

E-mail: iaoffice@jpl.nasa.gov

Refer to NPO-42481, volume and number of this NASA Tech Briefs issue, and the page number.



National Aeronautics and
Space Administration